

Co-Design of Low-Profile Linear Microstrip Arrays with Wide-Band Spatial Filtering Capabilities

A. Benoni,⁽¹⁾⁽²⁾ M. Salucci,⁽¹⁾⁽²⁾ *Senior Member, IEEE*, and A. Massa,⁽¹⁾⁽²⁾⁽³⁾⁽⁴⁾⁽⁵⁾ *Fellow, IEEE*

⁽¹⁾ *ELEDIA Research Center (ELEDIA@UniTN - University of Trento)*

DICAM - Department of Civil, Environmental, and Mechanical Engineering

Via Mesiano 77, 38123 Trento - Italy

E-mail: {arianna.benoni, marco.salucci, andrea.massa}@unitn.it

Website: www.eledia.org/eledia-unitn

⁽²⁾ *CNIT - "University of Trento" ELEDIA Research Unit*

Via Mesiano 77, 38123 Trento - Italy

E-mail: {arianna.benoni, marco.salucci, andrea.massa}@unitn.it

Website: www.eledia.org/eledia-unitn

⁽³⁾ *ELEDIA Research Center (ELEDIA@UESTC - UESTC)*

School of Electronic Science and Engineering, Chengdu 611731 - China

E-mail: andrea.massa@uestc.edu.cn

Website: www.eledia.org/eledia-uestc

⁽⁴⁾ *ELEDIA Research Center (ELEDIA@TSINGHUA - Tsinghua University)*

30 Shuangqing Rd, 100084 Haidian, Beijing - China

E-mail: andrea.massa@tsinghua.edu.cn

Website: www.eledia.org/eledia-tsinghua

⁽⁵⁾ *School of Electrical Engineering*

Tel Aviv University, Tel Aviv 69978 - Israel

E-mail: andrea.massa@eng.tau.ac.il

Website: <https://engineering.tau.ac.il/>

This work has been submitted to the IEEE for possible publication. Copyright may be transferred without notice, after which this version may no longer be accessible.

Co-Design of Low-Profile Linear Microstrip Arrays with Wide-Band Spatial Filtering Capabilities

A. Benoni, M. Salucci, and A. Massa

Abstract

The design of low-profile linear microstrip arrays with wide-band spatial filtering capabilities is dealt with. An innovative architecture, leveraging the angular selectivity of offset stacked patch (*OSP*) radiators, is proposed to implement phased arrays (*PAs*) with inter-element spacing larger than half-wavelength that feature remarkable grating lobes (*GLs*) suppression properties and an enhanced gain within a non-negligible down-looking scanning angular range. The *PA* layout is then obtained by optimizing the optimal *micro-scale* geometrical descriptors of the radiating elements so that the *macro-scale* electromagnetic (*EM*) features of the arising finite-size *PA* fulfill the user-defined requirements. A set of numerical test cases, concerned with a variation of the array size and its polarization, is presented to assess the capabilities, the flexibility, and the potentialities of the proposed spatial filtering technique (*SFT*) also in comparison with competitive state-of-the-art alternatives. The performance of a printed circuit board (*PCB*)-manufactured prototype are experimentally assessed, as well.

Key words: Phased Array (*PA*) Design; Spatial Filtering Techniques (*SFTs*); Grating Lobe (*GL*) Suppression; Offset Stacked Patches (*OSPs*); System-by-Design (*SbD*).

1 Introduction and Motivation

In modern communication and radar systems, phased arrays (*PAs*) have often to operate in complex environments where multiple radiating infrastructures, wireless devices, and sensors coexist [1]-[3]. Therefore, it is paramount to avoid interferences between the different systems. Towards this end, many practical scenarios require that the gain pattern of *PAs* fulfills a user-defined mask only within a limited scanning region depending on the targeted application [1][2]. For instance, interference mitigation/immunity of base transceiver stations (*BTSs*) is often improved by employing down-looking radiation patterns pointing towards the mobile end-users to yield an enhanced capacity and received signal strength [1]. While a mechanical tilting of the *BTS* antenna could in principle provide the desired performance, an electronic steering of the main beam direction is currently a preferred choice since it enables an easier reconfigurability to the changing operative/environmental conditions [1]-[7]. On the other hand, the need for high-directivity and low-cost antennas, fulfilling more and more challenging constraints when moving from current to next-generation standards [8][9], often implies the adoption of *PAs* with inter-element spacing larger than the conventional half-wavelength one without recurring to a more complex and expensive back-end circuitry and beam-forming network. Moreover, such a solution allows one to reduce the mutual coupling (*MC*) among the elementary radiators [3][5]-[7], as well. However, the “price to pay” is the unavoidable insurgence of grating lobes (*GLs*) in the array far-field (*FF*) pattern that correspond to spurious radiations towards above-the-horizon directions, while scanning the beam in elevation within the down-looking field-of-view (*FoV*) [3]. Such undesired phenomena cause a loss of both power and directivity [10][11] and they may generate unacceptable interferences towards geostationary satellites [3]. Therefore, the implementation of spatial filtering techniques (*SFTs*) to suppress undesired radiation towards unintended angular directions is of great interest [1]-[3][10]-[18]. Effective solutions have been recently proposed where the elementary radiators have been designed to radiate asymmetric patterns having higher gains within the angular scanning region of the array and lower gains where the *GLs* occur [1][2][14]. Thanks to such an “angular selectivity” of the radiators, it is thus possible to spatially filter out the *GLs* of the array pattern, while enhancing the array gain only within the desired *FoV*. For instance, asymmetric active element patterns have been

yielded in [1][14] by means of skewed dipoles (*SDs*) loaded with parasitic strips. Differently, electromagnetic band-gap (*EBG*) structures have been successfully exploited in [2] to tilt the radiation patterns of standard microstrip dipoles by properly tailoring the surface current distribution induced on their ground planes. Other promising solutions are those based on leaky-wave antennas (*LWAs*) built by placing a partially reflective surface (*PRS*) at a proper distance from the antenna aperture [10][11]. Alternatively, metasurface (*MTS*)-based lenses/domes have been recently designed to manipulate the *FF* pattern of the underlying *PAs* with anomalous refraction phenomena for mitigating the insurgence of *GLs* caused by an inter-element spacing larger than a half wavelength [3][12].

Although effective, the *SFT* implementations in the state-of-the-art literature are generally not low-profile. For instance, with reference to the illustrative sketch in Fig. 1, the antenna thickness turns out to be $T_{SD} = 0.7 [\lambda_c]$ in [1], $T_{EBG} = 0.84 [\lambda_c]$ in [2], $T_{PRS} = 0.46 [\lambda_c]$ in [11], and $T_{MTS} = 1.0 [\lambda_c]$ in [3], λ_c being the free-space wavelength at the central working frequency f_c . Moreover, some solutions are competitive only in narrow bandwidths (e.g., the fractional bandwidth of the *PRS*-based *SFT* in [11] is $FBW = 1.74\%$), and/or support limited *FoVs* (e.g., the maximum scan angle in [10] is $8.6 [\text{deg}]$), or they are designed for a fixed down-looking direction [2].

This work is aimed at presenting a simple, but rather effective, implementation of low-profile (i.e., $T_{OSP} < 0.15 [\lambda_c]$ - Fig. 1) linear microstrip arrays with wide-band spatial filtering capabilities. The proposed *PA* architecture exploits - for the first time to the best of the authors' knowledge - offset stacked patches (*OSPs*) [19]-[24], to design low-profile *PAs* with a remarkable *GLs* suppression and enhanced gain within a non-negligible down-looking angular scanning range. In order to synthesize robust and reliable array layouts, a *co-design* strategy [25] is introduced to take into account the effects of *MC* in the synthesis process for faithfully predicting the *FF* features of the arising finite-size *PA*.

The main novelties of this work over the existing literature consist, to the best of the authors' knowledge, in (i) the exploitation of *OSP* radiators, which are traditionally employed for bandwidth/gain enhancement [19]-[21] and/or *MC* reduction [22], as building blocks of low-profile microstrip *PAs* with spatial filtering capabilities and (ii) the solution of the *PA* synthesis problem

at hand with an innovative *co-design* strategy where the *micro-scale* descriptors of the elementary radiators are derived by directly optimizing the *macro-scale* electromagnetic (*EM*) features of the corresponding *PA*. As for this latter item (*ii*), the optimization problem is formulated within the System-by-Design (*SbD*) framework [26]-[29] to effectively cope with the computational burden caused by the need for repeated full-wave (*FW*) simulations of the whole finite size array instead of the single stand-alone *OSP* radiator.

The outline of the paper is as follows. Section 2 illustrates the proposed design concept and the working principle of the *OSP*-based architecture, while Section 3 describes the proposed co-design strategy within the *SbD* optimization framework. A representative set of numerical examples, concerned with the design of *PAs* of different sizes and polarizations, is discussed in Sect. 4 to illustrate the design/method features as well as to assess the effectiveness, the flexibility, and the high modularity of the proposed *SFT* solution also in comparison with competitive state-of-the-art alternatives. The *OSP*-based design concept is also experimentally verified with a *PCB*-manufactured prototype operating in the [24, 28] [GHz] *mm-wave* band (Sect. 5). Eventually (Sect. 6), some conclusions and final remarks are drawn.

2 Design Concept and Working Principle

Let us consider a linear array of N microstrip patches centered at $\{z_n = [\gamma - \lfloor \frac{N}{2} \rfloor + (n - 1)] \times d; n = 1, \dots, N\}$, where d is the uniform inter-element distance and $\gamma = \frac{1}{2}$ if $\text{mod}(N, 2) = 0$, $\gamma = 0$ otherwise, $\text{mod}(\cdot)$ and $\lfloor \cdot \rfloor$ being the modulo and the floor operators, respectively [Fig. 2(a)]. The *FF* electric field pattern radiated by the array is

$$\mathbf{E}(\theta, \varphi) = \sum_{q=\{\theta, \varphi\}} E_q(\theta, \varphi) \hat{\mathbf{q}} \quad (1)$$

where

$$E_q(\theta, \varphi) = \sum_{n=1}^N w_n \mathcal{E}_{nq}(\theta, \varphi) \exp \left[j \frac{2\pi}{\lambda} z_n \cos(\theta) \right] \quad (2)$$

is the q -th ($q = \{\theta, \varphi\}$) *FF* pattern component, which is a function of the n -th ($n = 1, \dots, N$) complex excitation coefficient [$w_n \triangleq \alpha_n \exp(j\beta_n)$] and the q -th ($q = \{\theta, \varphi\}$) active element

pattern of the n -th ($n = 1, \dots, N$) radiator, $\mathcal{E}_{nq}(\theta, \varphi)$ [30], λ being the free-space wavelength at the working frequency. It is useful to notice that for an array of isotropic elements [i.e., $\mathcal{E}_{nq}(\theta, \varphi) = \mathcal{E}_n(\theta, \varphi) = 1$; $n = 1, \dots, N$; $q = \{\theta, \varphi\}$], the *FF* electric field pattern coincides with the array factor $AF(\theta, \varphi)$ ($AF(\theta, \varphi) \triangleq \sum_{n=1}^N w_n \exp[j\frac{2\pi}{\lambda}z_n \cos(\theta)]$).

Let also the array be steered along the pointing direction θ_s with isophoric excitations, thus the amplitude and the phase of the n -th ($n = 1, \dots, N$) excitation turn out to be

$$\begin{aligned}\alpha_n &= 1 \\ \beta_n &= -\frac{2\pi}{\lambda}z_n \cos(\theta_s).\end{aligned}\tag{3}$$

Subject to the condition that $\frac{\lambda}{2} < d \leq \lambda$, a grating lobe (*GL*) appears in the (visible range of the) *AF* at the angular direction [5]

$$\theta_{GL} = \begin{cases} \arccos[\cos(\theta_s) + \frac{\lambda}{d}] & \text{if } 90 < \theta_s < 180 \text{ [deg]} \\ \arccos[\cos(\theta_s) - \frac{\lambda}{d}] & \text{if } 0 < \theta_s < 90 \text{ [deg]}, \end{cases}\tag{4}$$

which corresponds to a high side-lobe (*SL*) in the *FF* electric field pattern radiated by the array (1), that causes a loss of power and directivity. For instance, this is the case of a *BTS* array with the main beam pointed along a fixed down-looking angular direction $90 < \theta_s < 180$ [deg] that generates a significant *SL* directed towards the sky [i.e., $\theta_{GL} < 90$ [deg] - Fig. 2(a)], thus a potential interference with a satellite [1]-[3][13].

Ideally, to filter out the high *SL* appearing in the array pattern at $\theta = \theta_{GL}$ by also steering the main beam along θ_s , the q -th ($q = \{\theta, \varphi\}$) active element pattern of the n -th ($n = 1, \dots, N$) radiating element of the array should afford a maximum in correspondence with $\theta = \theta_s$, while having a null along the *GL* of the *AF* (i.e., $|\mathcal{E}_{nq}(\theta, \varphi)|_{\theta=\theta_{GL}; \varphi=0 \text{ [deg]}} = 0$) [1]-[3][13]. When dealing with real-array elements, an effective strategy to approximate such an ideal behavior is to mechanically tilt each radiator along the steering direction ($\theta_0 = \theta_s$, θ_0 being the tilt angle) so that the radiation above the horizon is minimized [i.e., $|\mathcal{E}_{nq}(\theta, \varphi)|_{\theta < 90, \varphi=0 \text{ [deg]}} < |\mathcal{E}_{nq}(\theta, \varphi)|_{\theta > 90, \varphi=0 \text{ [deg]}} \leq |\mathcal{E}_{nq}(\theta, \varphi)|_{\theta=\theta_0, \varphi=0 \text{ [deg]}}$ - Fig. 2(b)]. Such an asymmetric *angular selectivity* at the array-element level enables the spatial filtering of the *AF* by strongly limiting the power radiated by the array towards θ_{GL} and, as a by-product, enhancing it along θ_s [1]

[Fig. 2(b)]. However, the mechanical tilt of the array elements is a limiting factor for the implementation of low-profile structures.

Otherwise, the same effects on the radiated FF pattern can be also yielded by still acting on (i.e., steering) the element pattern, but without varying the orientation of the radiators to minimize the array thickness. Towards this end, *OSPs* [19]-[24] are used by exploiting their standard working principle, but for a purpose different from the standard one. Indeed, *OSPs* are generally designed either to improve the bandwidth of classical stacked patches (i.e., with the top parasitic element aligned with respect to the bottom excited element) [19]-[23] or to compensate the deviation of the pointing direction of probe-fed patches by displacing the upper parasitic radiator in the opposite direction to the feeding point [24]. Differently, they are here the technological recipe for building a low-profile microstrip radiator with tilted radiation pattern. More in detail, this paper considers a compact structure comprising $\mathcal{L} = 3$ stacked dielectric layers of relative permittivity ε_ℓ , loss tangent $\tan \delta_\ell$, and thickness t_ℓ ($\ell = 1, \dots, \mathcal{L}$) (Fig. 3). The two bottom layers ($\ell = 1, 2$) implement a linearly-polarized aperture-coupled patch where a rectangular slot of size $(L_s \times W_s)$ is etched in the ground plane on the top face of layer $\ell = 1$ with an offset O_s along the y -axis [Fig. 4(a)]. Such an aperture is fed by a microstrip line of length L_f and width W_f , which is terminated with an open-circuit stub and printed on the bottom face of the same layer [Fig. 4(a)]. The driven element is a rectangular patch of dimensions $(L_p \times W_p)$ on top of the layer $\ell = 2$ [Fig. 4(b)]. An offset parasitic patch is printed on the top layer of the antenna layout [i.e., $\ell = 3$ - Fig. 3 and Fig. 4(c)] to steer the radiation pattern of the radiator towards θ_0 ($\theta_0 > 90$ [deg]). Such a rectangular metallization, which is shifted by Δ_z along the negative z -axis [Fig. 4(c)] and having dimensions $(L_d \times W_d)$, acts as an offset “director” of the electromagnetic (EM) waves radiated by the underlying patch that deviate from the broadside direction ($\theta = 90$ [deg]) to generate an asymmetric element pattern with the desired spatial filtering capability [Fig. 3(b)].

3 Co-Design Strategy

Once the materials and thicknesses $\{(\varepsilon_\ell, \tan \delta_\ell, t_\ell); \ell = 1, \dots, \mathcal{L}\}$ have been chosen⁽¹⁾, the design problem is recast to retrieve the optimal setup of the K geometric descriptors (i.e., $\underline{\chi} = \{\chi_k; k = 1, \dots, K\}$, $K = 10$) of the *OSP* (Fig. 4)

$$\underline{\chi} = \{L_f, W_f, L_s, W_s, O_s, L_p, W_p, L_d, W_d, \Delta_z\} \quad (5)$$

to yield a suitable resonating behavior within the target frequency band B ($B \triangleq \{f_{\min} \leq f \leq f_{\max}\}$) as well as the desired spatial filtering properties when embedded in a linear array of identical elements.

It is worthwhile to notice that generally there are non-negligible differences, in terms of both input impedance and element pattern, between the *EM* behavior of the embedded radiator and the stand-alone one due to the unavoidable *MC* effects. Moreover, the active element pattern of each radiating element depends on its location within the aperture [30]. As a consequence, the synthesis of $\underline{\chi}$ based on the analysis of the *EM* features of a single *OSP* element radiating in free-space [Fig. 3(a)] may lead to unsatisfactory solutions once embedded in a linear arrangement. To yield a more robust and reliable solution, the set of *OSP micro-scale* descriptors (5) is determined through a co-design approach by directly optimizing the *macro-scale EM* features of the corresponding finite-size array. In other words, unlike forcing a proper impedance matching and a stand-alone *OSP* pattern towards $\theta_0 = \theta_s$, the design of the elementary radiator is carried out by requiring the embedded elements with *MC* to properly resonate in the target band, while lowering the sidelobe level (*SLL*) of the finite array when steering the main beam along θ_s . Towards this end, a global optimization is formulated by defining the following cost function

$$\Phi(\underline{\chi}) = \Phi_{EIM}(\underline{\chi}) + \Phi_{SLL}(\underline{\chi}). \quad (6)$$

In (6), Φ_{EIM} is the “embedded impedance matching” term, which enforces all the radiating

⁽¹⁾Among the off-the-shelf commercial products, the selection is driven by the user needs in terms of cost, robustness, and potential applications (e.g., terrestrial or space, environmental temperature/humidity).

elements of the array to resonate in the frequency-band B , given by

$$\Phi_{EIM}(\underline{\chi}) = \frac{1}{N \times B} \sum_{n=1}^N \int_{f_{\min}}^{f_{\max}} \frac{\mathcal{R}\{S_{nn}(f|\underline{\chi}) - S^{th}\}}{|S^{th}|} df \quad (7)$$

where S^{th} is a user-defined target threshold and $S_{nn}(f|\underline{\chi})$ is the reflection coefficient at the input port of the n -th ($n = 1, \dots, N$) array element, while $\mathcal{R}\{\cdot\}$ is the ramp function (i.e., $\mathcal{R}\{\xi\} = 1$ if $\xi > 0$, $\mathcal{R}\{\xi\} = 0$ otherwise).

The other term in (6) is devoted to counteract the occurrence of the GL (4) in the AF of the array. It is defined as follows

$$\Phi_{SLL}(\underline{\chi}) = \frac{1}{B} \int_{f_{\min}}^{f_{\max}} \frac{1}{|SLL(f|\underline{\chi})|} df, \quad (8)$$

$SLL(f|\underline{\chi})$ being the SLL of the array when setting its excitations to steer the main beam towards the user-defined down-looking angle $\theta = \theta_s$ (3).

Owing to both the high computational complexity of the synthesis problem at hand and the need for a faithful prediction of the EM behavior of the real finite array to assess through (6) the optimality of the antenna layout, the optimization [i.e., the minimization of (6)] is carried within the SbD framework [28][29]. More specifically, the PSO - OK/C implementation [28] of the SbD paradigm is here exploited to remarkably speed up the design process, while still keeping an accurate/reliable EM model of the array layout. It is based on the integration of a “*Solution Space Exploration*” (SSE) functional block, which leverages the particle swarm optimization (PSO) evolutionary operators [31][32], with an accurate/fast surrogate model (SM) of (6) relying on the Ordinary Kriging (OK) prediction technique [33][34][35]. To complete the whole optimization process (i.e., the building of the SM and the iterative PSO -based minimization of the OK -predicted cost function) within a fixed and limited amount of time, the SM is obtained by projecting the original solution space of the design variables (5) within a reduced one to minimize the size of the training set, thus reducing the number of computationally-expensive full-wave simulations of (6).

The co-design strategy can be summarized into the sequence of the following procedural steps:

1. *Input Phase* - Set the number of array elements, N , the inter-element distance d , and

the optimized down-looking elevation angle θ_s . Choose the dielectric materials and the thicknesses of the \mathcal{L} layers composing the *OSP* radiator. Set the desired *EIM* threshold S^{th} (7);

2. *SM Initialization* - Sample the K -dimensional space with the Latin hypercube sampling (*LHS*) technique [28][29] to generate B_0 trial designs $\{\underline{\chi}^{(b)}; b = 1, \dots, B_0\}$. Simulate each b -th ($b = 1, \dots, B_0$) design with a *FW* solver to compute its corresponding cost function, $\Phi(\underline{\chi}^{(b)})$ ($b = 1, \dots, B_0$). Train an *OK* model of the *EM* behavior of the *OSP* radiator by using the reduced-dimensionality database $\mathcal{D}_0 = \{[\mathfrak{N}(\underline{\chi}^{(b)}), \Phi(\underline{\chi}^{(b)})]; b = 1, \dots, B_0\}$ (\mathfrak{N} being the *PLS* operator [28]) to build a fast *SM*, $\tilde{\Phi}_0(\underline{\chi})$, of the cost function $\Phi(\underline{\chi})$ (6);
3. *SSE Initialization* ($i = 0$) - Initialize a swarm of P particles with random velocities $\mathcal{V}_0 = \{\underline{v}_0^{(p)}; p = 1, \dots, P\}$ and positions $\mathcal{P}_0 = \{\underline{\chi}_0^{(p)}; p = 1, \dots, P\}$ by setting

$$\underline{\chi}_0^{(1)} = \arg \left\{ \min_{b=1, \dots, B_0} [\Phi(\underline{\chi}^{(b)})] \right\} \quad (9)$$

and

$$\begin{cases} \underline{\chi}_0^{(p)} = \Psi \{ [\underline{\chi}^{(b)}; b = 1, \dots, B_0] \} \\ \underline{\chi}_0^{(p)} \neq \underline{\chi}_0^{(r)} \quad r = 1, \dots, p-1 \end{cases} \quad (10)$$

($p = 2, \dots, P$), $\Psi \{ \cdot \}$ being an operator randomly picking an entry from an input set;

4. *SSE Optimization* ($i = 1, \dots, I$) - Iteratively evolve the swarm positions by applying the *PSO-OK/C* updating rules [28]. At each i -th ($i = 1, \dots, I$) iteration select one trial solution $\underline{\chi}_i^{(*)}$ on the basis of the *OK* confidence level and predict its *EM* behavior with a *FW* solver to compute the corresponding cost function value $\Phi(\underline{\chi}_i^{(*)})$. Add such a new training sample to the database, $\mathcal{D}_i \leftarrow \mathcal{D}_{i-1} \cup \left[\mathfrak{N}(\underline{\chi}_i^{(*)}), \Phi(\underline{\chi}_i^{(*)}) \right]$, and update the size of the training set, $B_i \leftarrow (B_{i-1} + 1)$. Retrain the *OK* model with the updated database $\mathcal{D}_i = \{[\mathfrak{N}(\underline{\chi}^{(b)}), \Phi(\underline{\chi}^{(b)})]; b = 1, \dots, B_i\}$ to update the *SM*, $\tilde{\Phi}_i(\underline{\chi}) \leftarrow \tilde{\Phi}_{i-1}(\underline{\chi})$ for adaptively enhancing its prediction accuracy within the attraction basin of the global optimum of the cost function (6);
5. *Output Phase* - Output the optimal layout by setting $\underline{\chi}^{(opt)} = \arg \{ \min_{b=1, \dots, B} [\Phi(\underline{\chi}^{(b)})] \}$.

4 Numerical Assessment

This section is aimed at assessing the effectiveness and the potentialities of the proposed *SFT* in synthesizing low-profile linear microstrip arrays with wide-band spatial filtering capabilities. The first numerical experiment is concerned with the design of a linear *PA* of $N = 3$ horizontally-polarized (*H-Pol*) *OSP* elements, which are uniformly-spaced by $d = \lambda$, steered along $\theta_s = 110$ [deg] and operating within the frequency range B centered at $f_c = 28$ [GHz] and ranging from $f_{\min} = 26$ [GHz] up to $f_{\max} = 30$ [GHz] ($\rightarrow FBW = 14.3\%$, FBW being the fractional bandwidth), $S^{th} = -10$ [dB] being the admissibility threshold for the reflection coefficient. By choosing the *Taonic TLY* [*tm*] as dielectric material with $\varepsilon_\ell = 2.2$, $\tan \delta_\ell = 9 \times 10^{-4}$, and $t_\ell = 508$ [μm] ($\ell = 1, \dots, \mathcal{L}$), the *OSP* array layout has been forced to be low-profile with a total thickness T ($T \triangleq \sum_{\ell=1}^{\mathcal{L}} t_\ell$) of $T = 0.14$ [λ_c].

The co-design process has been carried out according to the procedure in Sect. 3 by setting the control parameters according to the literature guidelines [28]: $P = 10$ (P - swarm size), $I = 100$ (I - number of iterations), and $B_0 = 50$ (B_0 - size of the initial training set). Such a setup allowed a time saving of $\Delta t = 85\%$ [28] with respect to a standard *PSO*-based optimization that exploits only *FW* simulations⁽²⁾ for predicting the cost function values (6).

Figure 5 shows the arising array layout (*PA-OSP*) whose descriptors, $\underline{\chi}^{(opt)}$, are listed in Tab. I. The array properly resonates in the target band B as one can infer from Fig. 6(a) where the plot of the reflection coefficient at the input port of each n -th ($n = 1, \dots, N$) embedded *OSP* radiator is given. As a matter of fact, $S_{nn}(f) \leq -11.2$ [dB] ($n = 1, \dots, N$) when $f \in B$ and $S_{nn}(f_c) \leq -23.3$ [dB] ($n = 1, \dots, N$). Moreover, the *PA-OSP* features a remarkable spatial property as pointed out by the behavior of the normalized power pattern at $f = f_c$ [Fig. 6(b)]. Indeed, the *SLL* value turns out to be significantly smaller than that of an equally-spaced array of reference patches without offset directors (*PA-RP*). More in detail, the highest sidelobe appearing in the *PA-RP* pattern at $\theta_{SL} = 48.85$ [deg], which corresponds to the *GL* of the *AF* [i.e., $\theta_{SL} = \theta_{GL}$ (4)], is reduced by $\Delta SLL = 9.49$ [dB] ($\Delta SLL \triangleq SLL|_{PA-RP} - SLL|_{PA-OSP}$) from $SLL|_{PA-RP} = -2.96$ [dB] down to $SLL|_{PA-OSP} = -12.45$ [dB] [Fig. 6(b) and Tab. II]. Furthermore, the comparison of the *3D* gain patterns of both the *PA-OSP* [Fig. 7(a)] and the

⁽²⁾The *FW* Software Ansys *HFSS* [36] has been used to infer the *EM* behavior of the finite-size array.

PA-RP [Fig. 7(b)] highlight that, besides a *SLL* reduction, there is also an enhancement of the array gain in the steering direction of $\Delta G_s = 0.97$ [dB] [$\Delta G_s \triangleq G_s|_{PA-OSP} - G_s|_{PA-RP}$ being $G_s = G(\theta = \theta_s, \varphi = 0)$] (Tab. II).

As expected, the filtering features of the *PA-OSP* are the result of the angular selectivity of each elementary radiator that makes up the array (Fig. 8). As anticipated in Sect. 2, this arises from a tilting of all the embedded element (*EE*) patterns towards the array down-looking angular direction θ_s , which has been yielded in the co-design process without directly enforcing it in the cost function (6). Indeed, despite some slight angular shifts of the tilt angle θ_0 of the different radiators caused by the *MC* effects [i.e., $\theta_0^{(n)} \neq \theta_0^{(m)}$ ($n, m = 1, \dots, N; n \neq m$)], it turns out that $\theta_0^{(n)} \simeq \theta_s$ ($n = 1, \dots, N$) (Fig. 8), $G_s^{(n)} \geq 7.9$ [dB] ($n = 1, \dots, N$) being the gain along $\theta = \theta_s$ (Fig. 8). Such a tilting allows one to filter out the *GL* occurring in the *AF* thanks to the minimum of the radiation of the *OSP* radiators along $\theta = \theta_{GL}$ (Fig. 8), unlike the *RP* ones.

For completeness, Figure 9 shows the surface current distribution induced on the *PA-OSP* offset directors. On the one hand, the plot indicates that such parasitic metallizations have been properly excited, through proximity-coupling by the underlying driven patches, so that the power is radiated towards the down-looking direction of the array. On the other hand, as expected, the behavior of the induced current complies with the fundamental TM_{10} mode [37].

To point out the wide-band spatial filtering feature of the *PA-OSP*, Figure 10 plots the values of the *SLL* and of the gain within the operative band B . Despite the shift of the angular position of the *GL* when varying the frequency [$\theta_{GL} = 42.70$ [deg] at $f = f_{\min} = 26$ [GHz] - Fig. 11(a); $\theta_{GL} = 45.97$ [deg] at $f = 27$ [GHz] - Fig. 11(b); $\theta_{GL} = 51.43$ [deg] at $f = 29$ [GHz] - Fig. 11(c); $\theta_{GL} = 53.75$ [deg] at $f = f_{\max} = 30$ [GHz] - Fig. 11(d)], there is always a reduction of the *SLL* with respect to the *PA-RP* that amounts to $\Delta SLL|_{f=f_{\min}} = 4.75$ [dB] ($\Delta SLL|_{f=f_{\max}} = 7.51$ [dB]) at the lowest (highest) frequency of B (Fig. 10). The suppression of the sidelobes of the pattern radiated by the *PA-OSP* in the whole resonating spectrum is made evident by the representative pattern plots in Fig. 11, which are very similar to that in Fig. 6(b) for the central frequency. Moreover, the *PA-OSP* always yields a higher gain than the *PA-RP*, the improvement being equal to $\Delta G_s|_{f=f_{\min}} = 2.35$ [dB] ($\Delta G_s|_{f=f_{\max}} = 2.91$ [dB]) at the minimum (maximum) frequency (Fig. 10).

While the stand-alone optimization of the *OSP* radiator is unreliable for fulfilling the user-required *EM* behavior of the N -element array and its optimization in a large array is almost unfeasible from the computational viewpoint because of the use of a *FW EM* simulator, it is interesting to understand how effective is the *OSP* layout synthesized for a small array when arranged in a larger finite lattice of identical radiating elements. To address such a question, two linear *PA-OSPs* of $N = 5$ [Fig. 12(a)] and $N = 10$ [Fig. 12(b)] elements have been built using the same *OSP* radiator of the previous test case ($N = 3$). The results of this analysis are summarized in Fig. 12 and Tab. II. As it can be inferred, both the reduction of the *SLL* and the improvement of the array gain with respect to the *PA-RP* are of the same order in magnitude of the *PA* with $N = 3$ elements. Indeed, it turns out that ($\Delta SLL|_{N=5} = 9.77$ [dB]; $\Delta G_s|_{N=5} = 1.0$ [dB]) and ($\Delta SLL|_{N=10} = 10.97$ [dB]; $\Delta G_s|_{N=10} = 1.1$ [dB]) when $N = 5$ [Fig. 12(a) - Tab. II] and $N = 10$ [Fig. 12(b) - Tab. II], respectively.

Let us now focus on the largest aperture at hand (i.e., $N = 10$). Figure 13 shows the tilting of all the *EE-OSP* patterns towards θ_s analogously to the $N = 3$ case. Moreover, the plot of the *SLL* and of the gain versus the frequency in Fig. 14(a) confirms both the wide-band filtering capabilities and the higher gain of the *OSP*-array in the whole working band. It is also relevant to point out the robustness of the spatial filtering capabilities of the *PA-OSP* versus the scan angle, θ'_s , as highlighted in Fig. 14(b). Indeed, while the layout optimization has been carried out by setting the down-tilt of the array at $\theta_s = 110$ [deg], the plots of the *SLL* indicate that the *PA-OSP* overcomes the *PA-RP* (i.e., $SLL|_{PA-OSP} < SLL|_{PA-RP}$) in a wide portion of the scan range where $SLL < SLL_{th}$ ($SLL_{th} = 0$ [dB]). As a matter of fact, the threshold value SLL_{th} , which corresponds to the condition $G(\theta = \theta'_s) = G(\theta = \theta_{GL})$, is reached by the *PA-OSP* at a significantly greater value of the scan angle than that of the *PA-RP* [i.e., $\theta'_s|_{PA-OSP}^{th} = 146$ [deg] versus $\theta'_s|_{PA-RP}^{th} = 120$ [deg] - Fig. 14(b)]. On the other hand, there is a slight degradation of the *PA-OSP* performance as compared to the *PA-RP* one for the values of θ'_s close-to-the-horizon (i.e., 90 [deg] $\leq \theta'_s \leq 91.7$ [deg]) [Fig. 14(b)] since the *OSP* radiators have lower gains than the *RP* ones along broadside (i.e., $G^{(n)}(\theta)|_{OSP}^{\theta=90[\text{deg}]} \leq 7.7$ [dB] vs. $G^{(n)}(\theta)|_{RP}^{\theta=90[\text{deg}]} \leq 8.8$ [dB], $n = 1, \dots, N$ - Fig. 13). For illustrative purposes, the *FF* patterns at some representative values of the scan angle θ'_s [the plots at $\theta'_s = \theta_s = 110$ [deg] being in Fig. 12(b)] are reported in Fig.

15.

To further assess the generality of the proposed *SFT*, the next test case deals with the synthesis of a $N = 10$ elements vertically-polarized (*V-Pol*) *PA-OSP*. Towards this end, the co-design strategy (Sect. 3) has been applied to an array of *OSP* radiators rotated by 90 [deg] with respect to the layout in Figs. 3-4 to realize still a linear polarization, but orthogonal to that of the previous test cases. The layout synthesized when $\theta_s = 110$ [deg] is shown in Fig. 16, while the values of its geometric descriptors are reported in Tab. I. Once again, the *PA-OSP* pattern is significantly better than that of an equivalent-lattice *PA-RP* with the same polarization [Fig. 17(a)] since also quantitatively $\Delta SLL|_{V-Pol} = 11.63$ [dB] and $\Delta G_s|_{V-Pol} = 3.49$ [dB] (Tab. II). Similarly to the *H-Pol* case, such improvements are the result of the tilting of the embedded elementary patterns towards θ_s [Fig. 17(b)].

Finally, a comparison between the *V-Pol PA-OSP* in Fig. 16 and a *PA* steered at the same direction ($\theta_s = 110$ [deg]) with the same lattice/polarization, but composed by skewed dipoles (*PA-SD*) [1], has been carried out. The *FF* patterns in Fig. 18 show that the *SLL* is almost identical [i.e., $SLL|_{PA-OSP}^{\theta_s=110[\text{deg}]} = -12.85$ [dB] vs. $SLL|_{PA-SD}^{\theta_s=110[\text{deg}]} = -12.93$ [dB] - Figs. 18-19 and Tab. II], but the gain of the *PA-OSP* is remarkably higher (i.e., $G_s|_{PA-OSP}^{\theta_s=110[\text{deg}]} = 18.92$ [dB] vs. $G_s|_{PA-SD}^{\theta_s=110[\text{deg}]} = 16.39$ [dB] - Fig. 19 and Tab. II). Moreover, we cannot forget that the profile of the *PA-OSP* is significantly lower (i.e., $T_{PA-OSP} = 0.14$ [λ_c] vs. $T_{PA-SD} = 0.7$ [λ_c] [1] - Fig. 1) since no mechanical rotations of the elementary radiators are involved.

For completeness, the behavior of both the *SLL* and the gain versus θ'_s is shown in Fig. 19. As it can be inferred, the *PA-OSP* yields contemporarily a similar *SLL* and a higher gain than the *PA-SD* with the scanning range 103 [deg] $\leq \theta'_s \leq 134$ [deg], around the value used in the *PA-OSP* synthesis (i.e., $\theta_s = 110$ [deg]) ($\rightarrow -7$ [deg] $\leq \Delta\theta'_s \leq 24$ [deg], $\Delta\theta'_s \triangleq \theta'_s - \theta_s$).

5 Experimental Validation

To experimentally assess the effectiveness of the proposed *SFT* concept as well as the reliability of the co-design synthesis method, an *H-Pol PA-OSP* prototype with $N = 8$ elements operating at $f_c = 26$ [GHz] [$f \in [24, 28]$ [GHz] ($\rightarrow FBW = 15.4\%$)] has been realized via printed circuit board (*PCB*) manufacturing (Fig. 20). The bottom layer (ℓ_1) of the *PA-OSP* has been

realized with a Rogers *RO3003* material ($\varepsilon_1 = 3.0$, $\tan \delta_1 = 0.0013$) of thickness $t_1 = 130$ [μm], while the layers ℓ_2 and ℓ_3 have been implemented by using a Rogers/Duroid 5880 material ($\varepsilon_2 = \varepsilon_3 = 2.2$, $\tan \delta_2 = \tan \delta_3 = 0.009$) with thickness $t_2 = t_3 = 508$ [μm] ($\rightarrow T = 0.11$ [λ_c]). A corporate feeding network, able to feed the array elements with a fixed linear phase shifting to steer the main beam towards $\theta_s = 110$ [deg], has been etched on the bottom face of the layer ℓ_1 by cascading 2-ways power dividers and connecting them through 50 [Ω] microstrip lines [Fig. 20(b) and Fig. 20(d)]. For comparison, a linear *PA-RP* with the same number of array elements has been designed and prototyped by using the same substrates and beam-forming network (Fig. 21).

Figure 22 shows the magnitude of the reflection coefficient measured at the input connector (*RS PRO SMA 27G*) of both *PAs*. Both prototypes properly resonate in the target band (i.e., $|S_{11}(f)|_{PA-OSP}^{meas} \leq -11.6$ [dB] when $f \in B$ and $|S_{11}(f_c)|_{PA-OSP}^{meas} = -12.9$ [dB]⁽³⁾).

Concerning the radiation features, Figure 23(a) shows the plots of the measured co-polar patterns at $f = f_c$. One can notice that the undesired radiation towards θ_{GL} is considerably limited, the level of the sidelobes being reduced from $SLL|_{PA-RP}^{meas} = -2.3$ [dB] down to $SLL|_{PA-OSP}^{meas} = -11.6$ [dB] ($\rightarrow \Delta SLL^{meas} = 9.3$ [dB]) in close agreement with the simulations (i.e., $\Delta SLL^{sim} = 9.6$ [dB]).

Finally, Figure 23(b) gives a proof of the polarization purity of the array radiation by showing that the measured cross-polar (*CX*) level is $CX(\theta)|_{PA-OSP}^{meas} \leq -25.1$ [dB] within the range $\theta \in [0, 180]$ [deg], while $CX(\theta)|_{PA-RP}^{meas} \leq -24.2$ [dB].

6 Conclusions

An innovative *SFT* for implementing low-profile linear microstrip *PAs* with inter-element spacing larger than half-wavelength has been presented. The proposed architecture exploits *OSP* radiators to implement an angular selectivity suitable for suppressing the undesired *PA* radiation caused by the insurgence of *GLs* in the corresponding *AF*. To provide a reliable and robust design, which takes into account the *MC* effects arising in real/finite-size arrays, a *co-design* ap-

⁽³⁾The deviations of the measured S_{11} values from the simulated ones (Fig. 22) are due to several non-idealities in the manufacturing process as well as to the presence of spurious reflections caused by the soldered connector [Figs. 20(c)-20(d) and Fig. 21(b)].

proach has been introduced where the *micro-scale* descriptors of the elementary *OSP* radiator are optimized to fulfill the requirements on the *macro-scale EM* performance of the corresponding *PA*.

The main outcomes from the numerical and experimental assessment have been the following ones:

- the proposed *SFT* yields a remarkable control of the *SLL* of the *PA* over a wide-band (e.g., $FBW = 14.3\%$);
- the *OSP-PA* still guarantees a non-negligible suppression of the *GLs* also when steering the beam towards down-looking directions different from the optimized one;
- it is possible (i.e., the performance are still acceptable) to build linear arrays of different size (i.e., a different number of array elements) without the need for re-optimizing the layout of the *OSP* radiator for each *PA* arrangement;
- both the *PA* architecture and the co-design method can be seamlessly used to synthesize *H-Pol* as well as *V-Pol* linear arrays;
- the *OSP-PA* solution positively compares with a leading-edge state-of-the-art solution [1] in terms of spatial filtering capabilities and gain values, while exhibiting a lower profile;
- the *FW*-simulated performance and the *EM* behavior of the proposed *OSP-PA* architecture are experimentally confirmed by a *PCB*-manufactured prototype operating in the *mm*-wave band $24 [\text{GHz}] \leq f \leq 28 [\text{GHz}]$.

Future works, beyond the scope of this paper, will be aimed at extending the proposed *SFT* to both planar arrangements and dual-polarizations (e.g., slant-45) operation [3].

Acknowledgements

This work benefited from the networking activities carried out within the Project Project “Hub Life Science - Advanced Diagnosis (HLS-AD), PNRR PNC-E3-2022-23683266 PNC-HLS-DA, INNOVA” funded by the Italian Ministry of Health under the National Complementary

Plan Innovative Health Ecosystem (CUP: E63C22003780001 - Unique Investment Code: PNC-E.3), the Project “AURORA - Smart Materials for Ubiquitous Energy Harvesting, Storage, and Delivery in Next Generation Sustainable Environments” funded by the Italian Ministry for Universities and Research within the PRIN-PNRR 2022 Program (CUP: E53D23014760001), the Project “Telecommunications of the Future” (PE00000001 - program “RESTART”, Structural Project 6GWINET), funded by European Union under the Italian National Recovery and Resilience Plan (NRRP) of NextGenerationEU (CUP: D43C22003080001), and the Project DICAM-EXC (Grant L232/2016) funded by the Italian Ministry of Education, Universities and Research (MUR) within the “Departments of Excellence 2023-2027” Program (CUP: E63C22003880001). The authors are very grateful to Prof. R. Azaro (EMC s.r.l., Via Greto di Cornigliano, 6/r, 16152 GENOVA - emc.info@emclab.it) for the prototyping and the experimental measurements. A. Massa wishes to thank E. Vico for her never-ending inspiration, support, guidance, and help.

References

- [1] C. Yepes, E. Gandini, S. Monni, A. Neto, F. E. van Vliet, and D. Cavallo, “A linear array of skewed dipoles with asymmetric radiation pattern for angular filtering,” *IEEE Antennas Wireless Propag. Lett.*, vol. 19, no. 3, pp. 408-412, Mar. 2020.
- [2] I. Kim and Y. Rahmat-Samii, “Electromagnetic band gap-dipole sub-array antennas creating an enhanced tilted beams for future base station,” *IET Microw. Antennas Propag.*, vol. 9, no. 4, pp. 319-327, Mar. 2015.
- [3] D. Ramaccia, M. Barbuto, A. Monti, S. Vellucci, C. Massagrande, A. Toscano, and F. Bilotti, “Metasurface dome for above-the-horizon grating lobes reduction in 5G-NR systems,” *IEEE Antennas Wireless Propag. Lett.*, 2022, vol. 21, no. 11, pp. 2176-2180, Nov. 2022.
- [4] P. Rocca, G. Oliveri, R. J. Mailloux, and A. Massa, “Unconventional phased array architectures and design methodologies - A review,” *Proc. IEEE*, vol. 104, no. 3, pp. 544-560, Mar. 2016.

- [5] C. Balanis, *Antenna theory: analysis and design*. Hoboken, N.J.: Wiley, 2016.
- [6] J. S. Herd and M. David Conway, "The evolution to modern phased array architectures," *Proc. IEEE*, vol. 104, no. 3, pp. 519-529, 2016.
- [7] R. J. Mailloux, *Phased Array Antenna Handbook* (3rd ed). Norwood, MA, USA: Artech House, 2018.
- [8] C. Cox, *An Introduction to 5G: The New Radio, 5G Network and Beyond*. Hoboken, NJ, USA: John Wiley & Sons, 2021.
- [9] H. Tataria, M. Shafi, A. F. Molisch, M. Dohler, H. Sjoland, and F. Tufvesson, "6G wireless systems: Vision, requirements, challenges, insights, and opportunities," *Proc. IEEE*, vol. 109, no. 7, pp. 1166-1199, Jul. 2021.
- [10] D. Blanco, N. Llombart, and E. Rajo-Iglesias, "On the use of leaky wave phased arrays for the reduction of the grating lobe level," *IEEE Trans. Antennas Propag.*, vol. 62, no. 4, pp. 1789-1795, Apr. 2014.
- [11] D. Blanco, E. Rajo-Iglesias, A. M. Benito, and N. Llombart, "Leaky-wave thinned phased array in PCB technology for telecommunication applications," *IEEE Trans. Antennas Propag.*, vol. 64, no. 10, pp. 4288-4296, Oct. 2016.
- [12] M. Jiang, Z. N. Chen, Y. Zhang, W. Hong, and X. Xuan, "Metamaterial-based thin planar lens antenna for spatial beamforming and multibeam massive MIMO," *IEEE Trans. Antennas Propag.*, vol. 65, no. 2, pp. 464-472, Feb. 2017.
- [13] L. H. Ye, X. Y. Zhang, Y. Gao, and Q. Xue, "Wideband dual-polarized two-beam antenna array with low sidelobe and grating-lobe levels for base-station applications," *IEEE Trans. Antennas Propag.*, vol. 67, no. 8, pp. 5334-5343, Aug. 2019.
- [14] C. Yepes, E. Gandini, S. Monni, A. Neto, F. E. van Vliet, and D. Cavallo, "Analysis of tilted dipole arrays: Impedance and radiation properties," *IEEE Trans. Antennas Propag.*, vol. 68, no. 1, pp. 254-265, Jan. 2020.

- [15] Y. J. Lee, S. H. Jeong, W. S. Park, J. S. Yun, and S. I. Jeon, "Multilayer spatial angular filter with airgap tuners to suppress grating lobes of 4×1 array antenna," *Electron. Lett.*, vol. 39, no. 1, pp. 15-17, Jan. 2003.
- [16] Y. J. Lee, J. Yeo, R. Mittra, and W. S. Park, "Application of electromagnetic bandgap (EBG) superstrates with controllable defects for a class of patch antennas as spatial angular filters," *IEEE Trans. Antennas Propag.*, vol. 53, no. 1, pp. 224-235, Jan. 2005.
- [17] Z. Iqbal and M. Pour, "Grating lobe reduction in scanning phased array antennas with large element spacing," *IEEE Trans. Antennas Propag.*, vol. 66, no. 12, pp. 6965-6974, Dec. 2018.
- [18] Z. Iqbal and M. Pour, "Exploiting higher order modes for grating lobe reduction in scanning phased array antennas," *IEEE Trans. Antennas Propag.*, vol. 67, no. 11, pp. 7144-7149, Nov. 2019.
- [19] E. Rajo-Iglesias, G. Villaseca-Sanchez, and C. Martin-Pascual, "Input impedance behavior in offset stacked patches," *IEEE Antennas Wireless Propag. Lett.*, vol. 1, pp. 28-30, 2002.
- [20] V. P. Sarin, M. S. Nishamol, D. Tony, C. K. Aanandan, P. Mohanan, and K. Vasudevan, "A wideband stacked offset microstrip antenna with Improved gain and low cross polarization," *IEEE Trans. Antennas Propag.*, vol. 59, no. 4, pp. 1376-1379, Apr. 2011.
- [21] A. Katyal and A. Basu, "Analysis and optimisation of broadband stacked microstrip antennas using transmission line model," *IET Microw. Antennas Propag.*, vol. 11, no. 1, pp. 81-91, Jan. 2017.
- [22] A. Katyal and A. Basu, "Compact and broadband stacked microstrip patch antenna for target scanning applications," *IEEE Antennas Wireless Propag. Lett.*, vol. 16, pp. 381-384, 2017.
- [23] K. M. Luk, K. F. Tong, and T. M. Au, "Offset dual-patch microstrip antenna," *Electron. Lett.*, vol. 29, no. 18, pp. 1635-1636, Sep. 1993.

- [24] E. Rajo-Iglesias, J.-L. Vazquez-Roy, L. Inclan-Sanchez, D. Segovia-Vargas, V. Gonzalez-Posadas, and C. Martin-Pascual, "Offset stacked patches behavior in an array," *Microw. Opt. Technol. Lett.*, vol. 40, no. 3, pp. 262-265, Dec. 2003.
- [25] G. Oliveri, G. Gottardi, F. Robol, A. Polo, L. Poli, M. Salucci, M. Chuan, C. Massagrande, P. Vinetti, M. Mattivi, R. Lombardi, and A. Massa, "Codesign of unconventional array architectures and antenna elements for 5G base stations," *IEEE Trans. Antennas Propag.*, vol. 65, no. 12, pp. 6752-6767, Dec. 2017.
- [26] G. Oliveri, M. Salucci, N. Anselmi, and A. Massa, "Multiscale system-by-design synthesis of printed WAIMs for waveguide array enhancement," *IEEE J. Multiscale Multiphysics Computat. Techn.*, vol. 2, pp. 84-96, 2017.
- [27] G. Oliveri, A. Polo, M. Salucci, G. Gottardi, and A. Massa, "SbD-Based synthesis of low-profile WAIM superstrates for printed patch arrays," *IEEE Trans. Antennas Propag.*, vol. 69, no. 7, pp. 3849-3862, Jul. 2021.
- [28] A. Massa and M. Salucci, "On the design of complex *EM* devices and systems through the System-by-Design paradigm - A framework for dealing with the computational complexity," *IEEE Trans. Antennas Propag.*, vol. 70, no. 2, pp. 1328-1343, Feb. 2022.
- [29] M. Salucci, G. Oliveri, M. A. Hannan, and A. Massa, "System-by-Design paradigm-based synthesis of complex systems: The case of spline-contoured 3D radomes," *IEEE Antennas Propag. Mag.*, vol. 64, no. 1, pp. 72-83, Feb. 2022.
- [30] D. M. Pozar, "The active element pattern," *IEEE Trans. Antennas Propag.*, vol. 42, no. 8, pp. 1176-1178, Aug. 1994.
- [31] P. Rocca, M. Benedetti, M. Donelli, D. Franceschini, and A. Massa, "Evolutionary optimization as applied to inverse scattering problems," *Inv. Prob.*, vol. 24, pp. 1-41, 2009.
- [32] S. K. Goudos, *Emerging Evolutionary Algorithms for Antennas and Wireless Communications*. IET, 2021 (ISBN 1785615521).

- [33] A. Massa, G. Oliveri, M. Salucci, N. Anselmi, and P. Rocca, "Learning-by-examples techniques as applied to electromagnetics," *J. Electromagn. Waves Appl.*, vol. 32, no. 4, pp. 516-541, 2018.
- [34] A. I. J. Forrester, A. Sobester, and A. J. Keane, *Engineering Design via Surrogate Modelling: A Practical Guide*. Hoboken, N.J.: John Wiley & Sons, 2008.
- [35] D. R. Jones, M. Schonlau, and W. J. Welch, "Efficient global optimization of expensive black-box functions," *J. Global Opt.*, vol. 13, pp. 455-492, 1998.
- [36] ANSYS Electromagnetics Suite - HFSS (2021). ANSYS, Inc.
- [37] P. Perlmutter, S. Shtrikman, and D. Treves, "Electric surface current model for the analysis of microstrip antennas with application to rectangular elements," *IEEE Trans. Antennas Propag.*, vol. 33, no. 3, pp. 301-311, Mar. 1985.

FIGURE CAPTIONS

- **Figure 1.** Linear array layouts.
- **Figure 2.** Pictorial sketch of a linear array of d -spaced ($d > \frac{\lambda}{2}$) microstrip (a) patches and (b) offset stacked patches.
- **Figure 3.** Layout of (a) the *OSP* radiator and (b) the uniform linear array of N *OSP* radiators.
- **Figure 4.** Top view of the ℓ -th layer of the *OSP* radiator: $\ell = 1$, (b) $\ell = 2$, and (c) $\ell = 3$.
- **Figure 5.** Numerical Assessment (*H-Pol*, $N = 3$, $\theta_s = 110$ [deg]) - CAD model of the synthesized *PA-OSP*.
- **Figure 6.** Numerical Assessment (*H-Pol*, $N = 3$, $\theta_s = 110$ [deg]) - Plots of (a) the reflection coefficient at the input port of each n -th ($n = 1, \dots, N$) embedded *OSP* radiator versus the frequency and (b) the normalized power pattern at $f = f_c$ along with the *AF* and the *EE* pattern of the central element ($n = 2$) of both the *PA-RP* and the *PA-OSP* in the elevation cut ($\varphi = 0$ [deg]).
- **Figure 7.** Numerical Assessment (*H-Pol*, $N = 3$, $\theta_s = 110$ [deg], $f = f_c = 28$ [GHz]) - Simulated 3D gain pattern of (a) the *PA-OSP* and (b) the *PA-RP* arrays.
- **Figure 8.** Numerical Assessment (*H-Pol*, $N = 3$, $\theta_s = 110$ [deg], $f = f_c = 28$ [GHz]) - Simulated gain patterns of the N elements of both the *PA-RP* and the *PA-OSP*.
- **Figure 9.** Numerical Assessment (*H-Pol*, $N = 3$, $\theta_s = 110$ [deg], $f = f_c = 28$ [GHz]) - Simulated distribution of the surface current excited on the offset directors of the *PA-OSP* in Fig. 5.
- **Figure 10.** Numerical Assessment (*H-Pol*, $N = 3$, $\theta_s = 110$ [deg]) - Behavior of the *SLL* and of the gain (G_s) versus the frequency f for both the *PA-RP* and the *PA-OSP*.
- **Figure 11.** Numerical Assessment (*H-Pol*, $N = 3$, $\theta_s = 110$ [deg]) - Plot in the elevation cut ($\varphi = 0$ [deg]) of the normalized power pattern along with the *AF* and the *EE* pattern

of the central element ($n = 2$) of both the *PA-RP* and the *PA-OSP* at (a) $f = f_{\min} = 26$ [GHz], (b) $f = 27$ [GHz], (c) $f = 29$ [GHz], and (d) $f = f_{\max} = 30$ [GHz].

- **Figure 12.** *Numerical Assessment (H-Pol, $\theta_s = 110$ [deg], $f = f_c = 28$ [GHz])* - Plot in the elevation cut ($\varphi = 0$ [deg]) of the normalized power pattern along with the *AF* and the *EE* pattern of the central element of both the *PA-RP* and the *PA-OSP* with (a) $N = 5$ and (b) $N = 10$ elements.
- **Figure 13.** *Numerical Assessment (H-Pol, $N = 10$, $\theta_s = 110$ [deg], $f = f_c = 28$ [GHz])* - Simulated gain patterns of the N elements of both the *PA-RP* and the *PA-OSP*.
- **Figure 14.** *Numerical Assessment (H-Pol, $N = 10$, $\theta_s = 110$ [deg])* - Behavior of the *SLL* and of the gain (G_s) for both the *PA-RP* and the *PA-OSP* versus (a) the frequency f and (b) the scan angle θ'_s .
- **Figure 15.** *Numerical Assessment (H-Pol, $N = 10$, $f = f_c = 28$ [GHz], $\theta_s = 110$ [deg])* - Plot in the elevation cut ($\varphi = 0$ [deg]) of the normalized power pattern along with the *AF* and the *EE* pattern of the central element of both the *PA-RP* and the *PA-OSP* when steering the main beam towards (a) $\theta'_s = 90$ [deg] ($\rightarrow \theta_{GL} = 0.0$ [deg]), (b) $\theta'_s = 100$ [deg] ($\rightarrow \theta_{GL} = 34.3$ [deg]), and (c) $\theta'_s = 140$ [deg] ($\rightarrow \theta_{GL} = 76.5$ [deg]).
- **Figure 16.** *Numerical Assessment (V-Pol, $N = 10$, $\theta_s = 110$ [deg])* - CAD model of the synthesized *PA-OSP*.
- **Figure 17.** *Numerical Assessment (V-Pol, $N = 10$, $\theta_s = 110$ [deg], $f = f_c = 28$ [GHz])* - Plot in the elevation cut ($\varphi = 0$ [deg]) of (a) the normalized power pattern along with the *AF* and the *EE* pattern of the central element of both the *PA-RP* and the *PA-OSP* and (b) the gain patterns of the N elements of the *PA-OSP*.
- **Figure 18.** *Numerical Assessment (V-Pol, $N = 10$, $\theta_s = 110$ [deg], $f = f_c = 28$ [GHz])* - Plot in the elevation cut ($\varphi = 0$ [deg]) of the normalized power pattern along with the *AF* and the *EE* pattern of the central element of both the *PA-SD* [1] and the *PA-OSP*.
- **Figure 19.** *Numerical Assessment (V-Pol, $N = 10$, $\theta_s = 110$ [deg], $f = f_c = 28$ [GHz])*

- Behavior of the *SLL* and of the gain (G_s) versus the scan angle θ'_s for the *PA-SD* [1], the *PA-RP*, and the *PA-OSP*.
- **Figure 20.** *Experimental Assessment (H-Pol, $N = 8, \theta_s = 110$ [deg])* - Pictures of (a)(c) the top and (b)(d) the bottom views of the (a)(b) *FW*-simulated model and (c)(d) the *PCB*-manufactured prototype of the *PA-OSP*.
- **Figure 21.** *Experimental Assessment (H-Pol, $N = 8, \theta_s = 110$ [deg], $f = f_c = 26$ [GHz])* - Pictures of the top view of the (a) *FW*-simulated model and (b) the *PCB*-manufactured prototype of the *PA-RP*.
- **Figure 22.** *Experimental Assessment (H-Pol, $N = 8, \theta_s = 110$ [deg], $f \in [22, 30]$ [GHz])* - Simulated and measured values of the reflection coefficient at the input port of both the *PA-OSP* and the *PA-RP*.
- **Figure 23.** *Experimental Assessment (H-Pol, $N = 8, \theta_s = 110$ [deg], $f = f_c = 26$ [GHz])* - Simulated and measured (a) co-polar and (b) cross-polar patterns radiated by the *PA-OSP* and the *PA-RP*.

TABLE CAPTIONS

- **Table I.** *Numerical Assessment ($d = \lambda, [f_{\min}, f_{\max}] = [26, 30]$ [GHz], $\theta_s = 110$ [deg])* - Optimized values of the *OSP* descriptors (5).
- **Table II.** *Numerical Assessment ($d = \lambda, [f_{\min}, f_{\max}] = [26, 30]$ [GHz], $\theta_s = 110$ [deg], $f = f_c = 28$ [GHz])* - *SLL* and gain values.

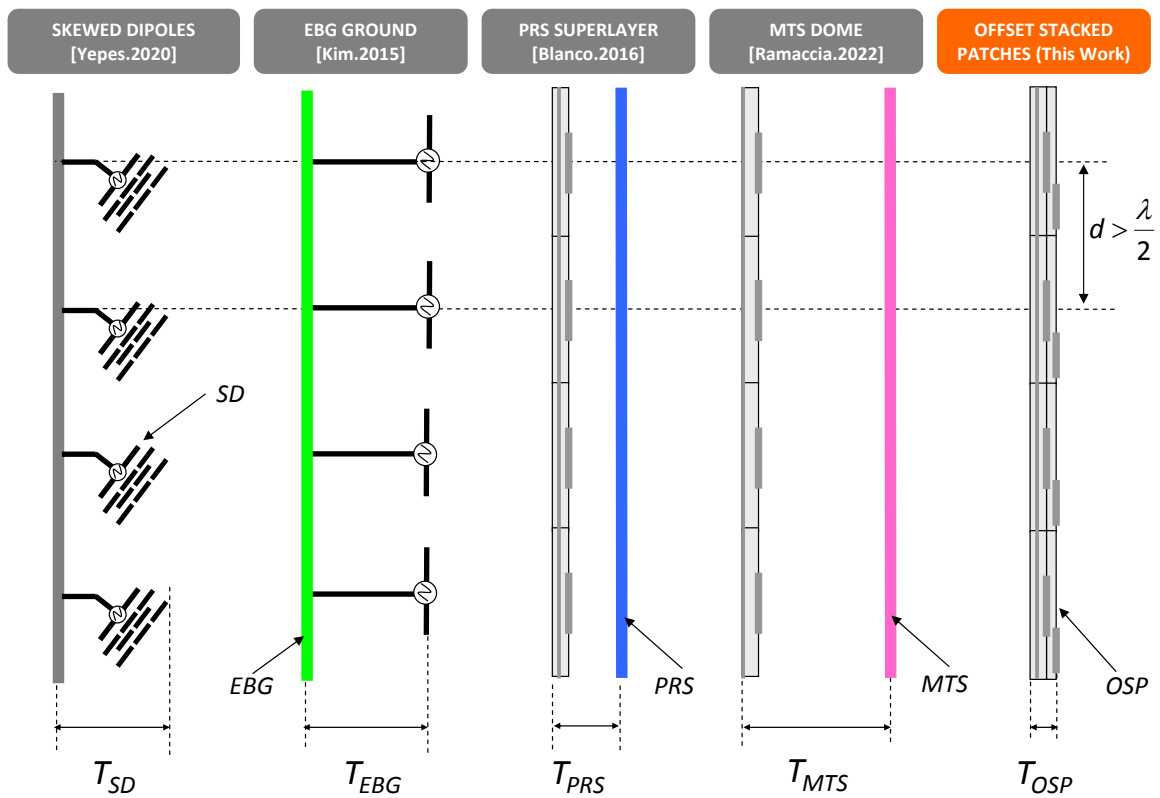
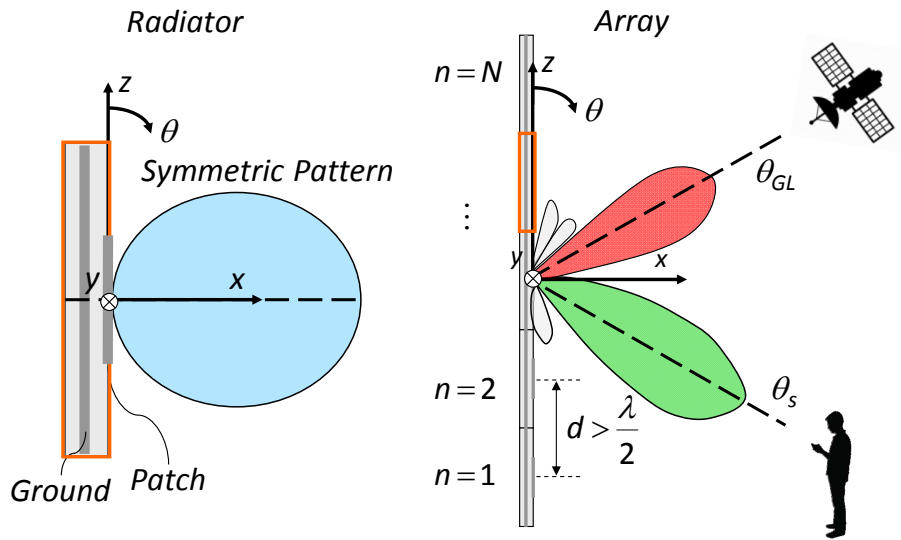
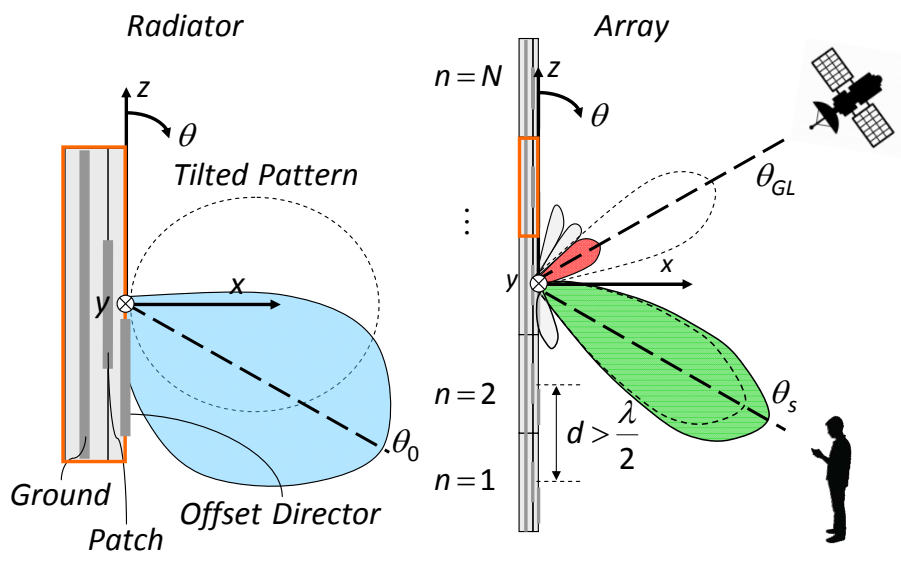


Fig. 1 - A. Benoni et al., “Co-Design of Low-Profile Linear Microstrip Arrays ...”

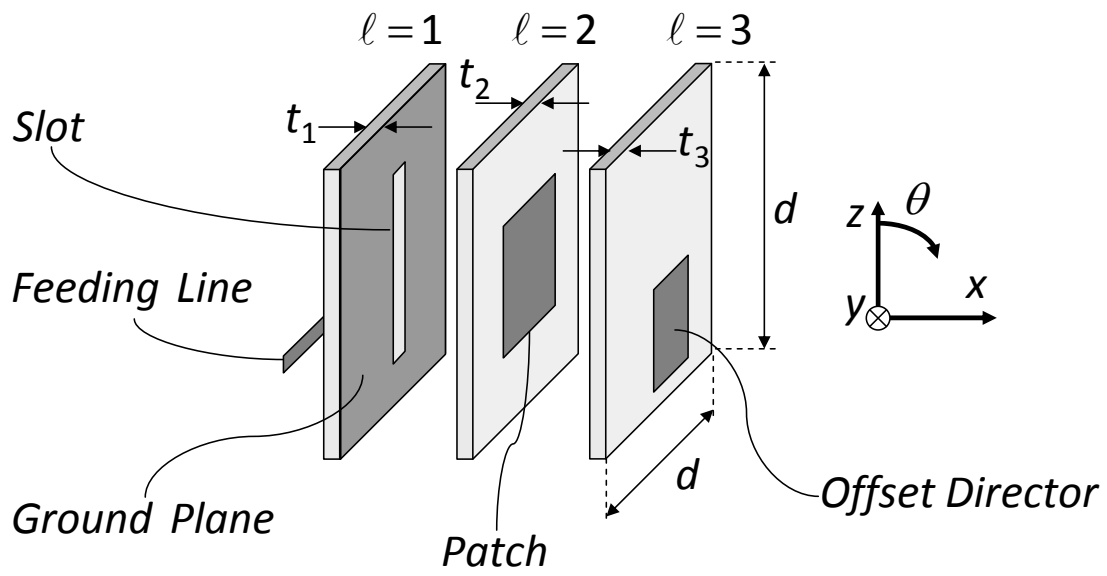


(a)

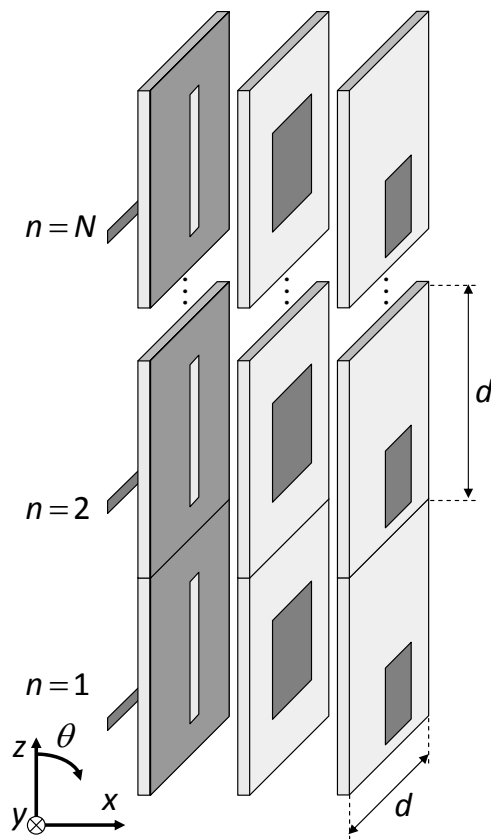


(b)

Fig. 2 - A. Benoni et al., "Co-Design of Low-Profile Linear Microstrip Arrays ..."



(a)



(b)

Fig. 3 - A. Benoni et al., "Co-Design of Low-Profile Linear Microstrip Arrays ..."

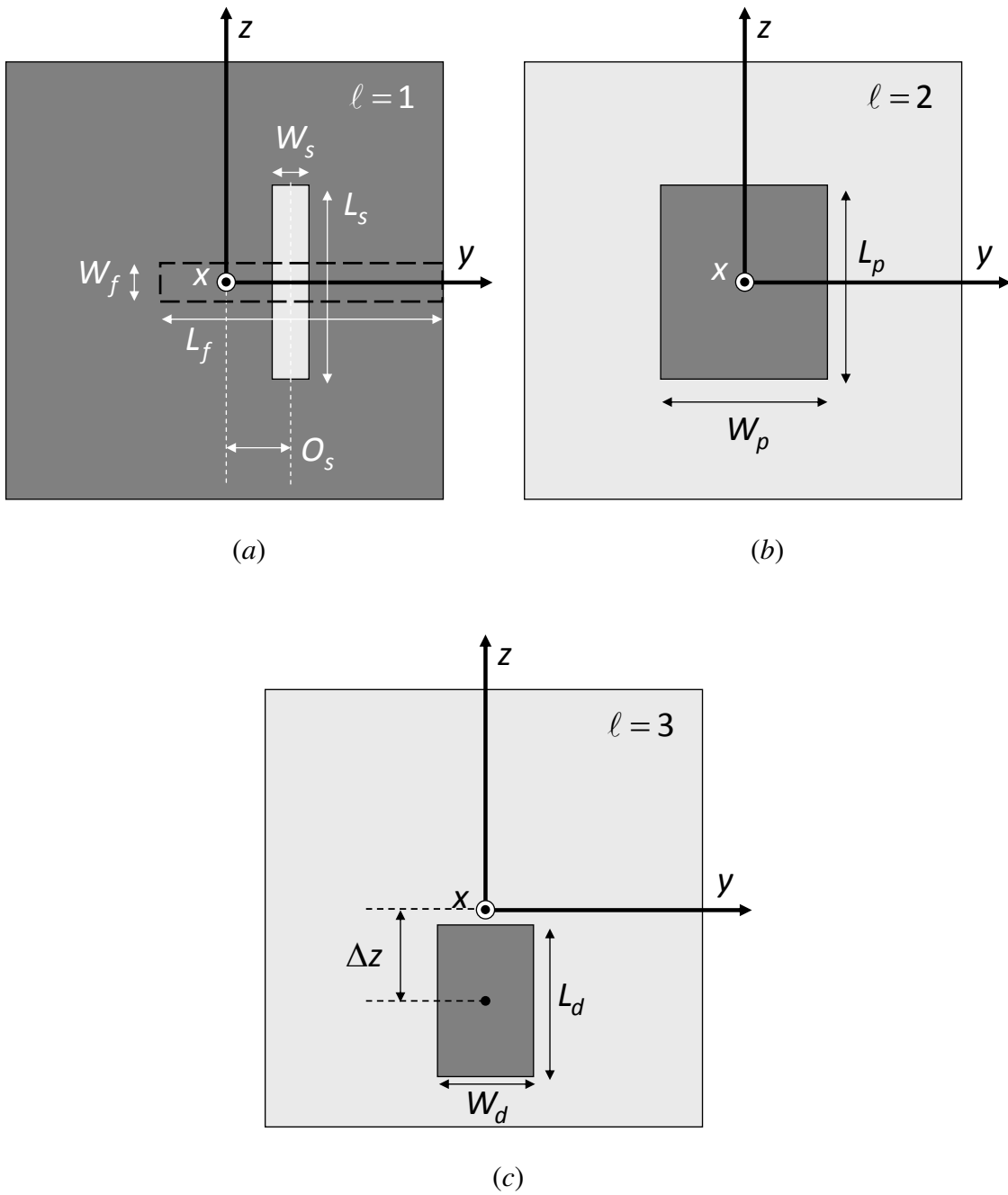


Fig. 4 - A. Benoni et al., “Co-Design of Low-Profile Linear Microstrip Arrays ...”

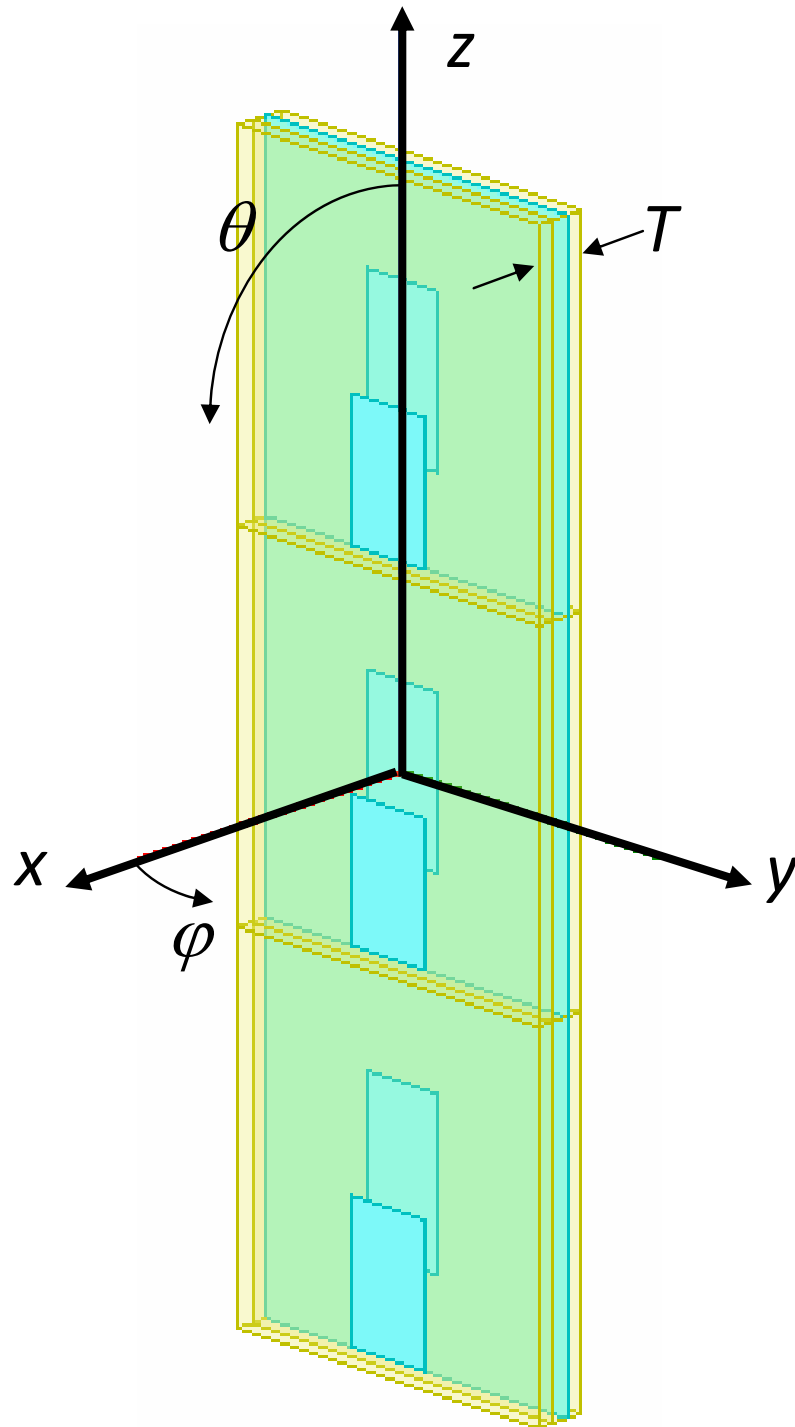


Fig. 5 - A. Benoni et al., "Co-Design of Low-Profile Linear Microstrip Arrays ..."

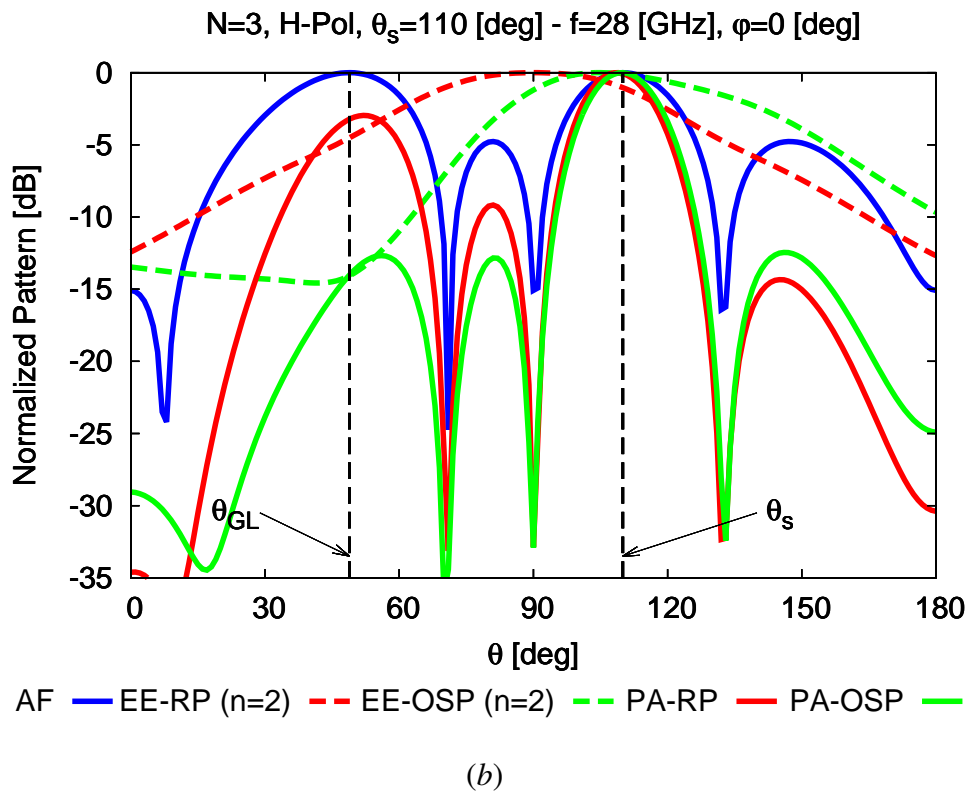
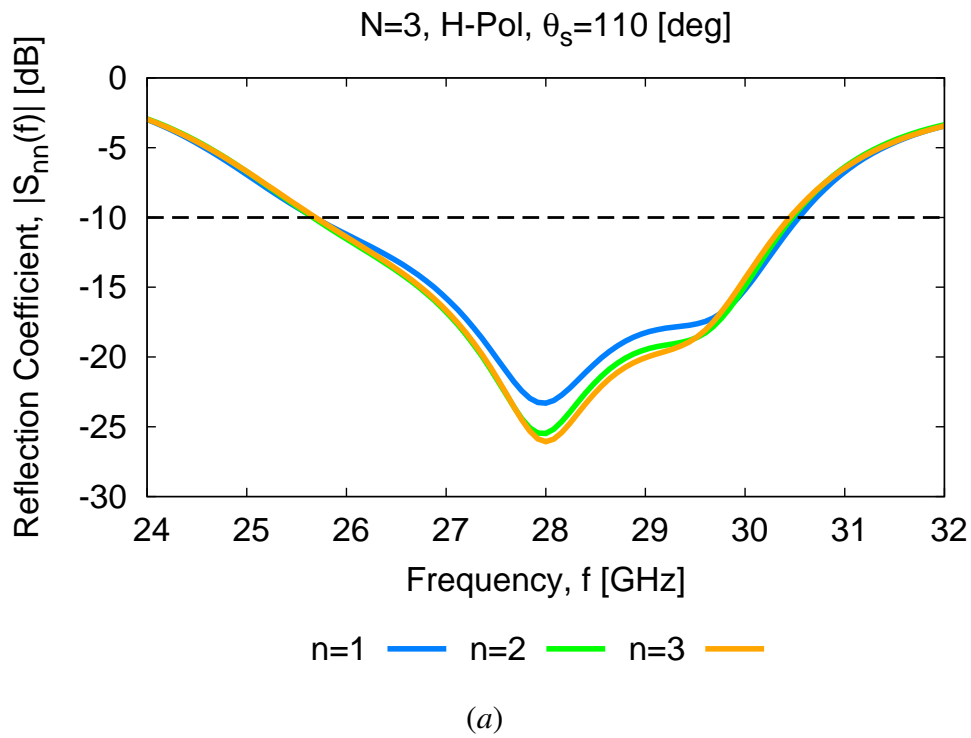
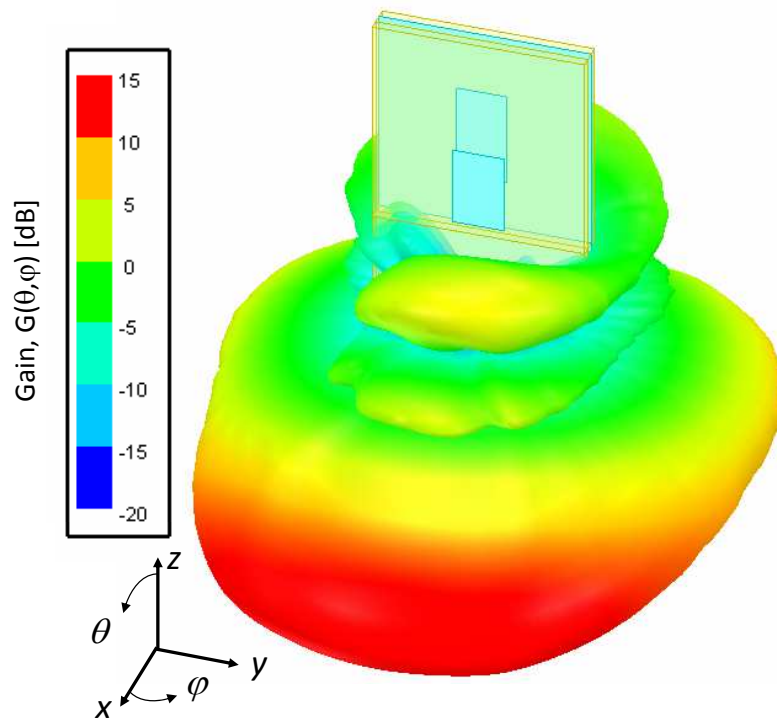
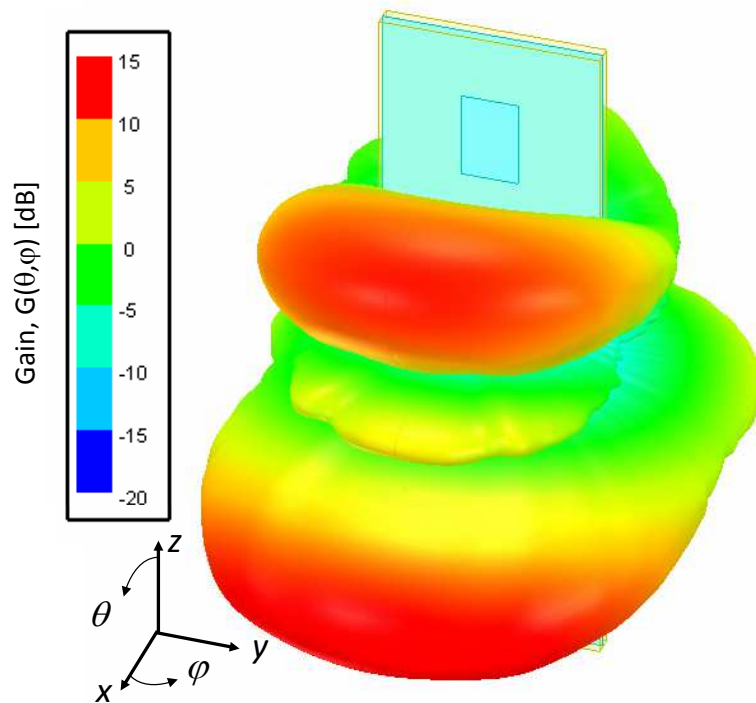


Fig. 6 - A. Benoni et al., “Co-Design of Low-Profile Linear Microstrip Arrays ...”



(a)



(b)

Fig. 7 - A. Benoni et al., "Co-Design of Low-Profile Linear Microstrip Arrays ..."

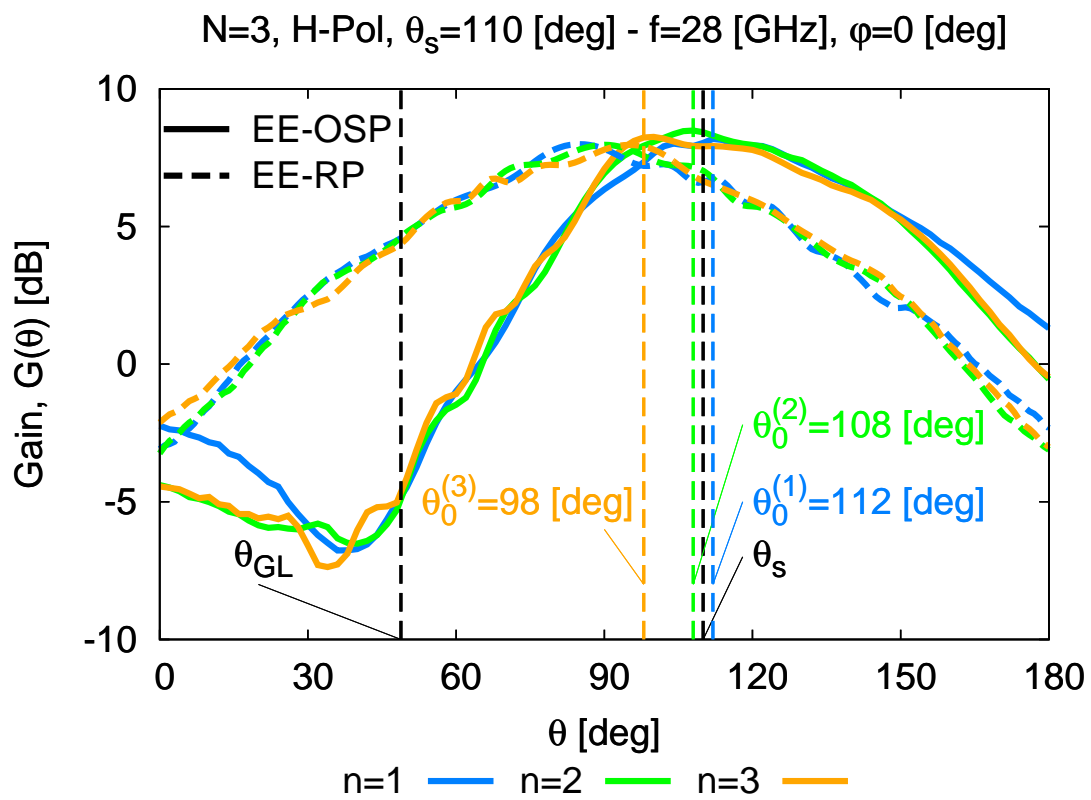


Fig. 8 - A. Benoni et al., “Co-Design of Low-Profile Linear Microstrip Arrays ...”

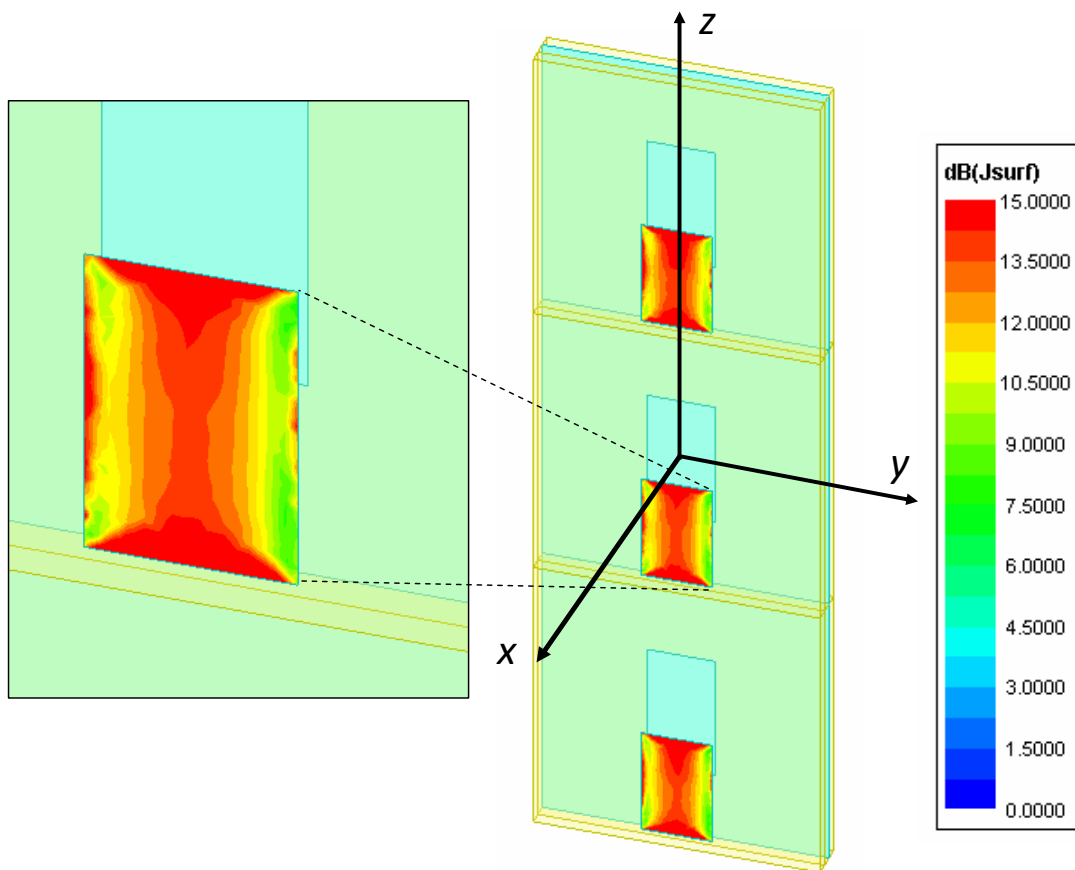


Fig. 9 - A. Benoni et al., “Co-Design of Low-Profile Linear Microstrip Arrays ...”

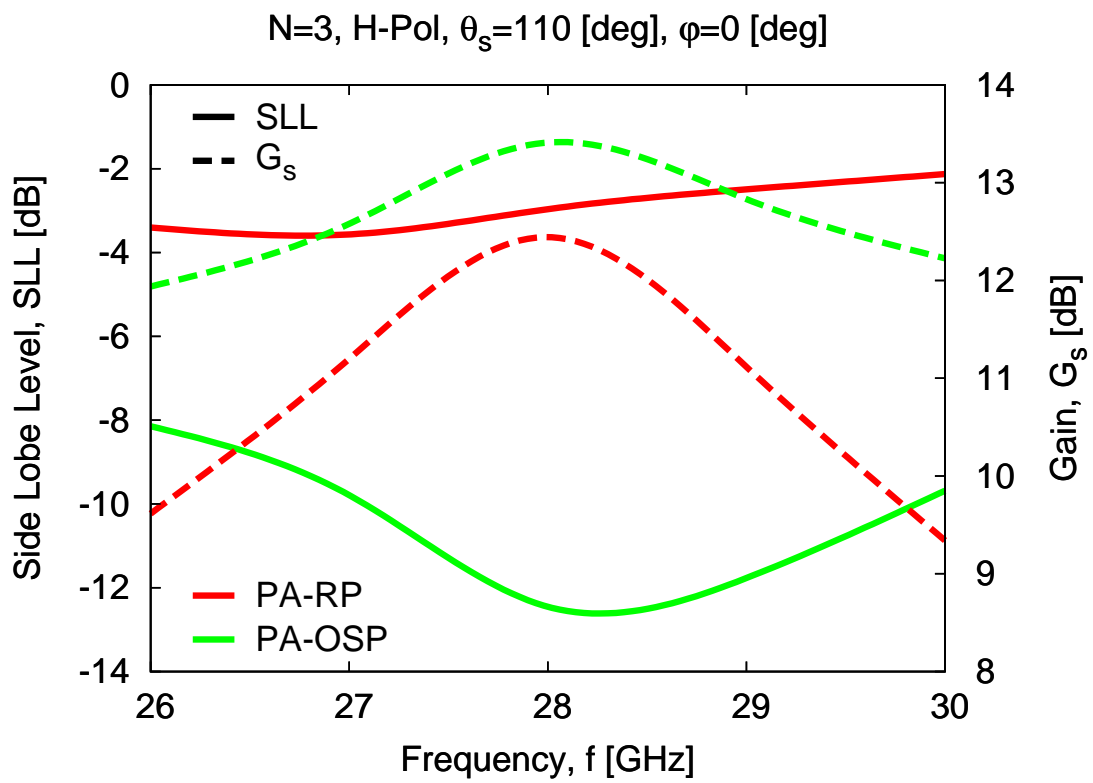


Fig. 10 - A. Benoni et al., “Co-Design of Low-Profile Linear Microstrip Arrays ...”

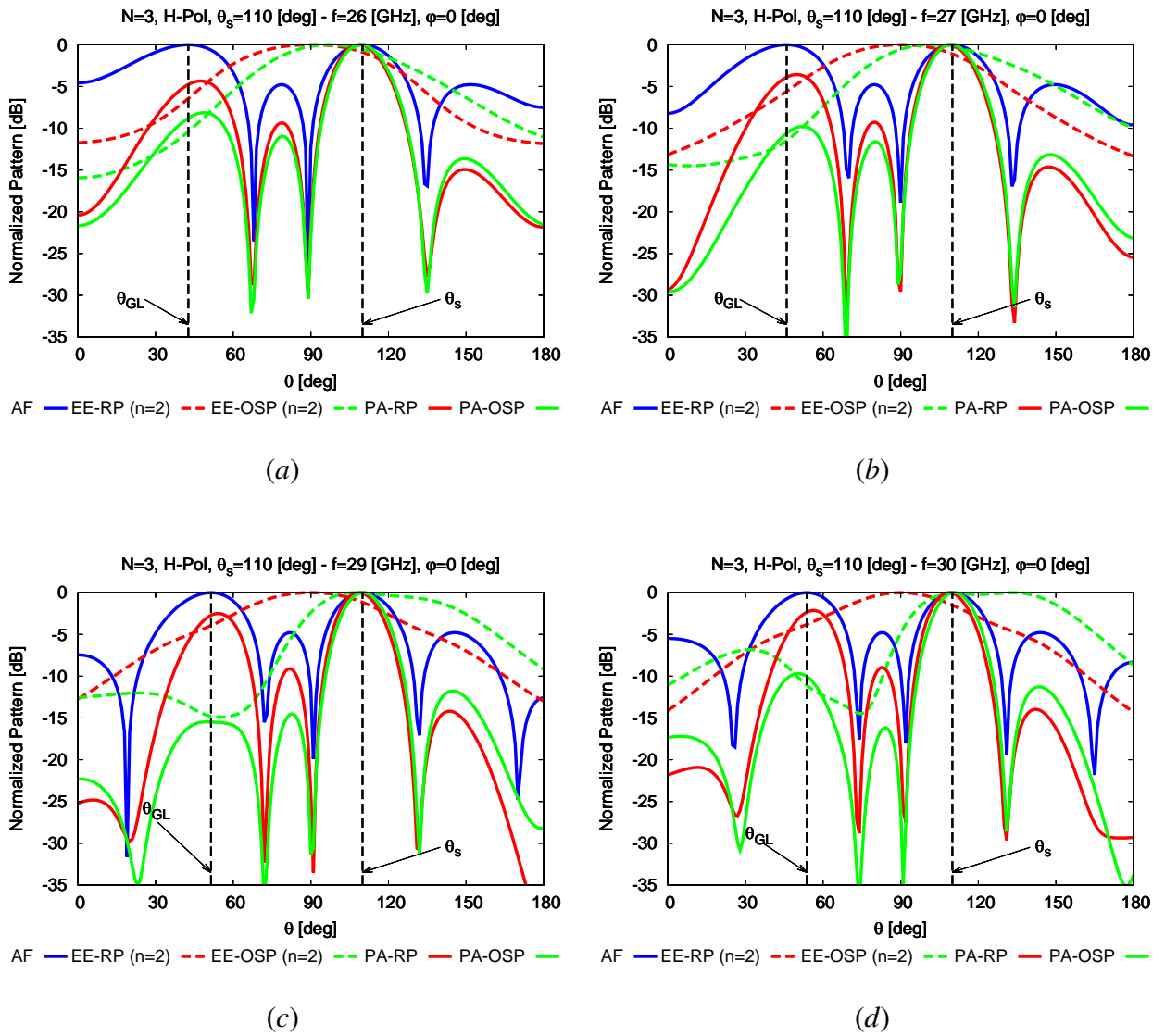
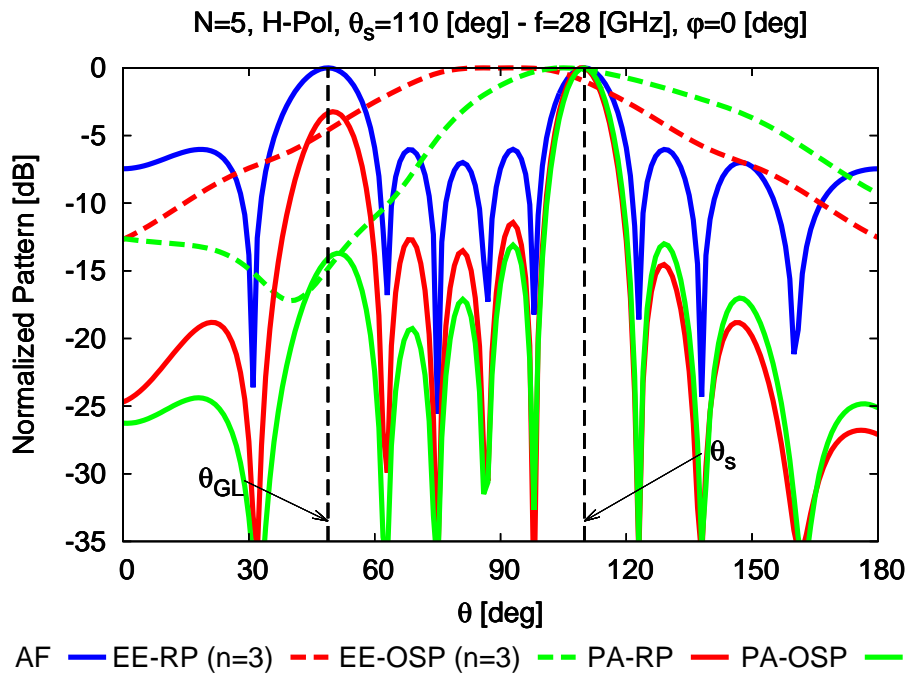
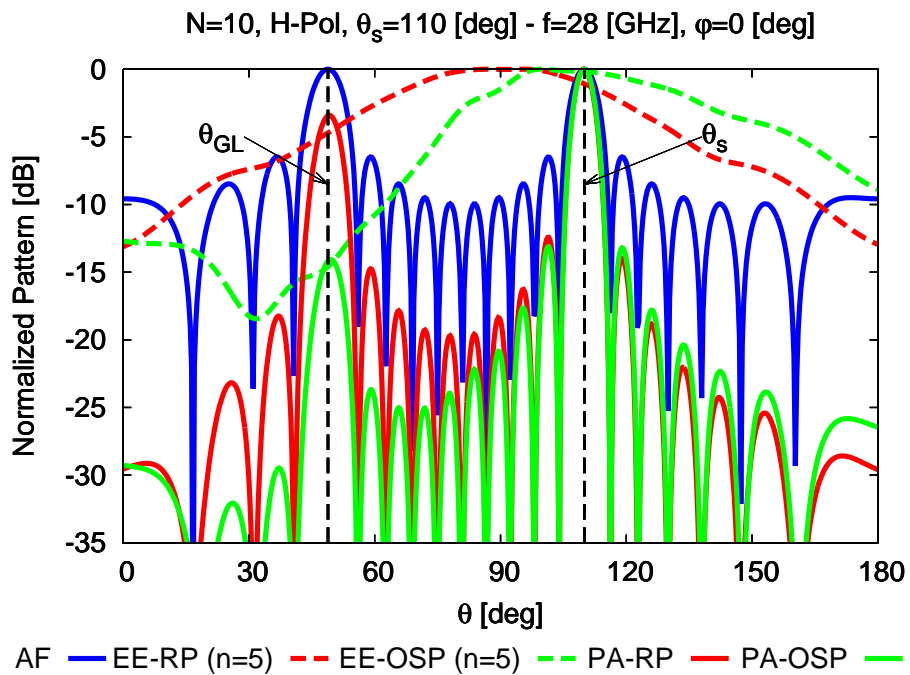


Fig. 11 - A. Benoni et al., "Co-Design of Low-Profile Linear Microstrip Arrays ..."



(a)



(b)

Fig. 12 - A. Benoni et al., “Co-Design of Low-Profile Linear Microstrip Arrays ...”

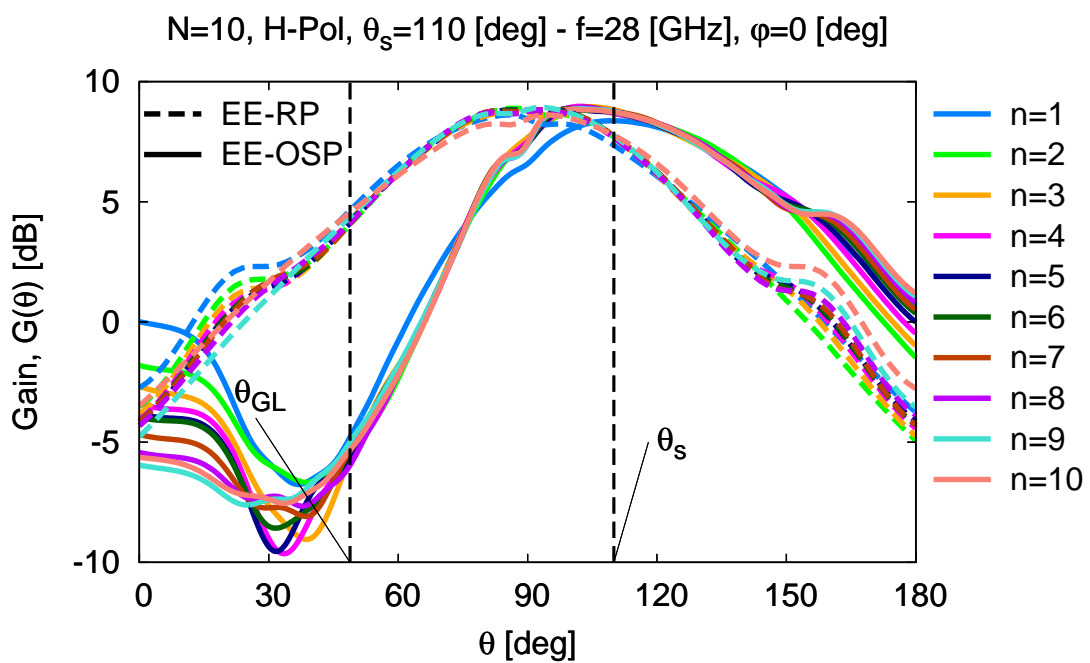


Fig. 13 - A. Benoni et al., “Co-Design of Low-Profile Linear Microstrip Arrays ...”

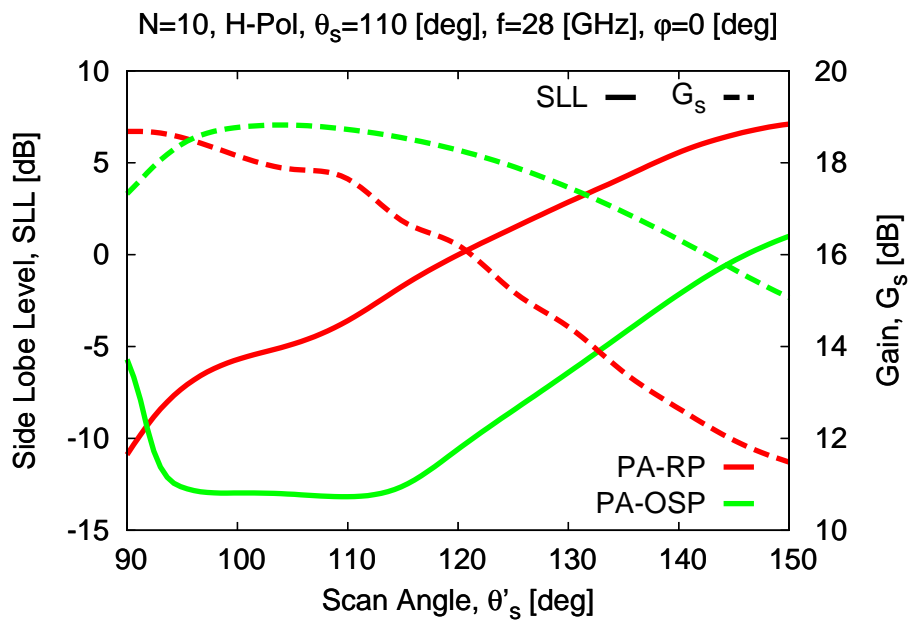
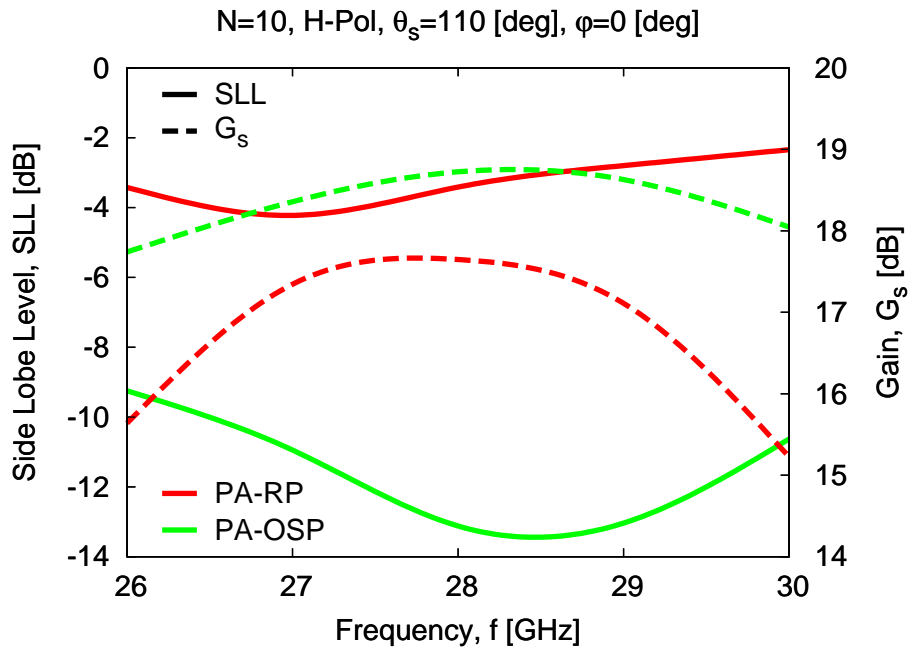
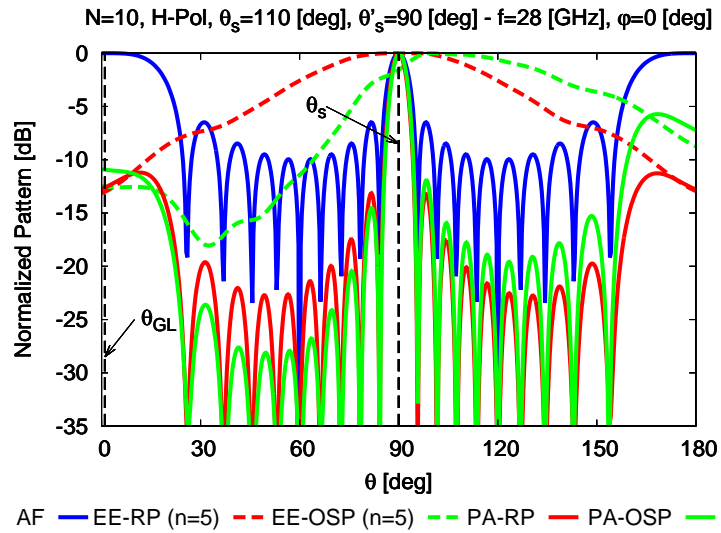
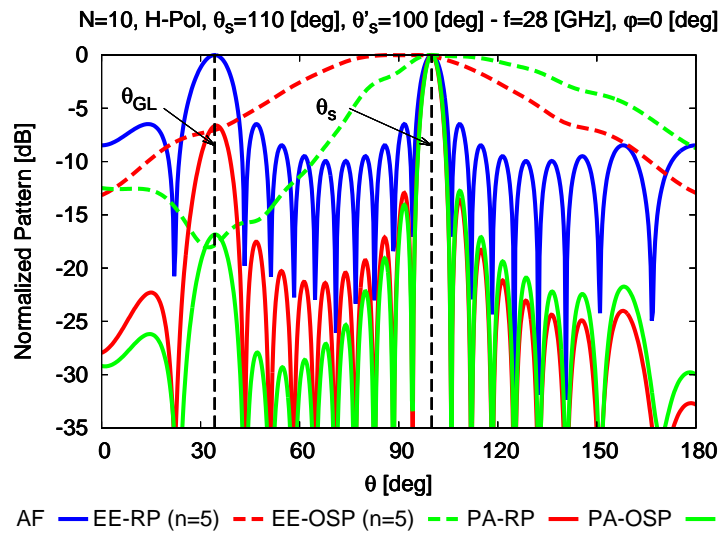


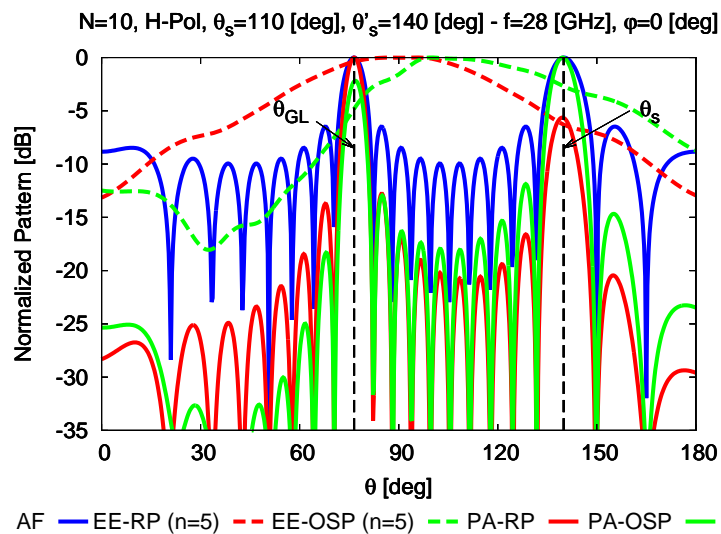
Fig. 14 - A. Benoni et al., “Co-Design of Low-Profile Linear Microstrip Arrays ...”



(a)



(b)



(c)

Fig. 15 - A. Benoni et al., “Co-Design of Low-Profile Linear Microstrip Arrays ...”

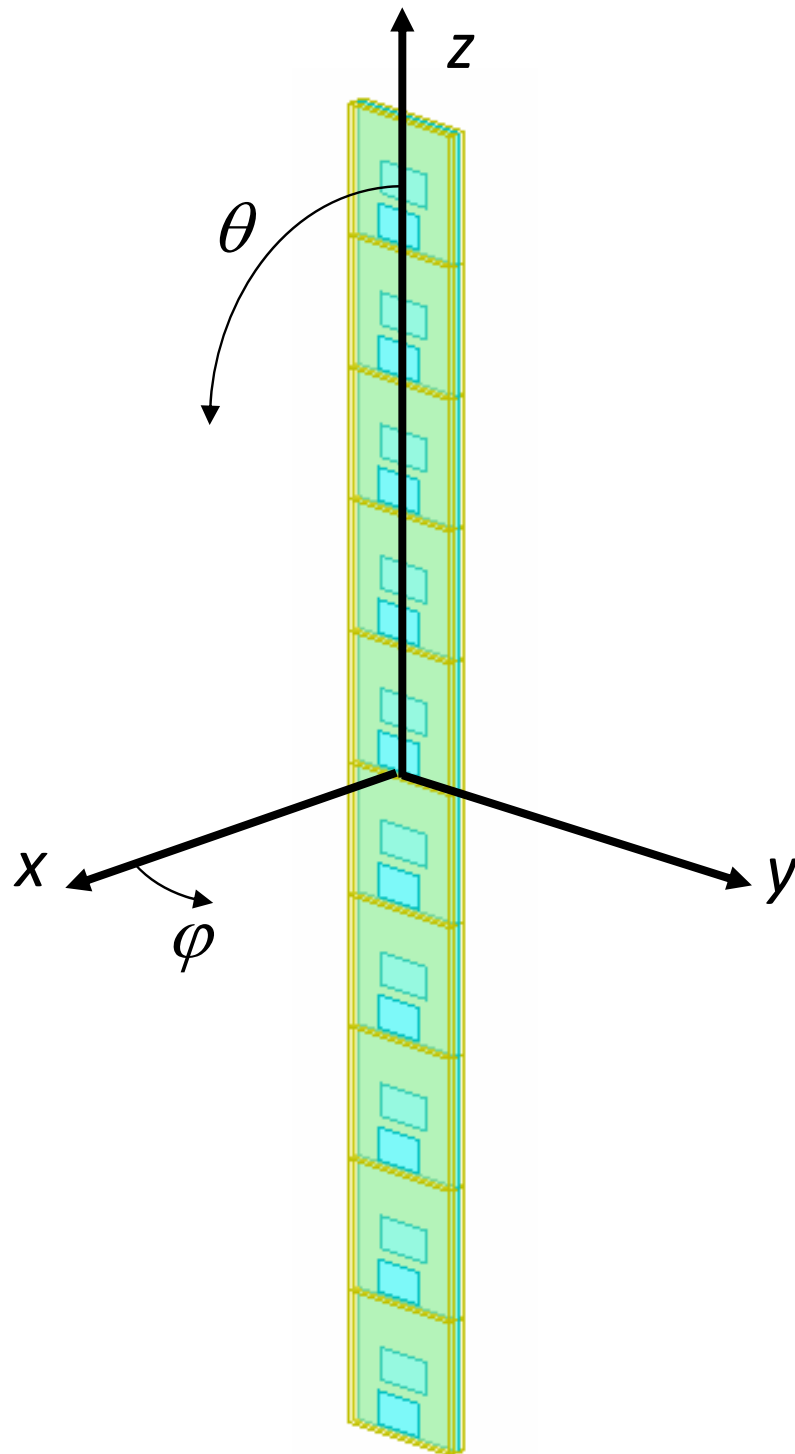
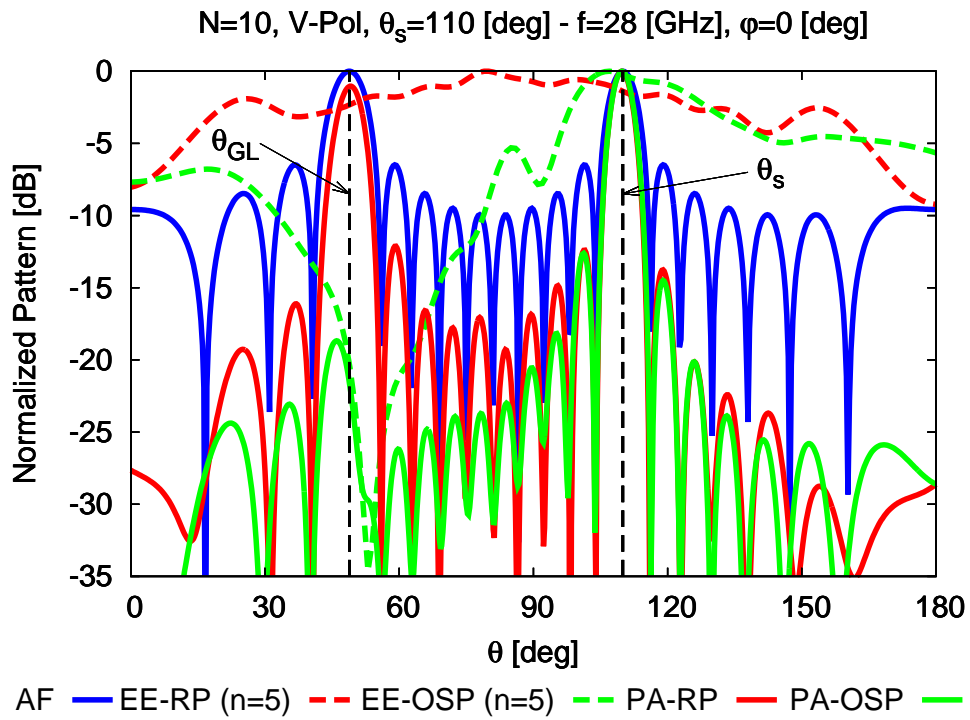
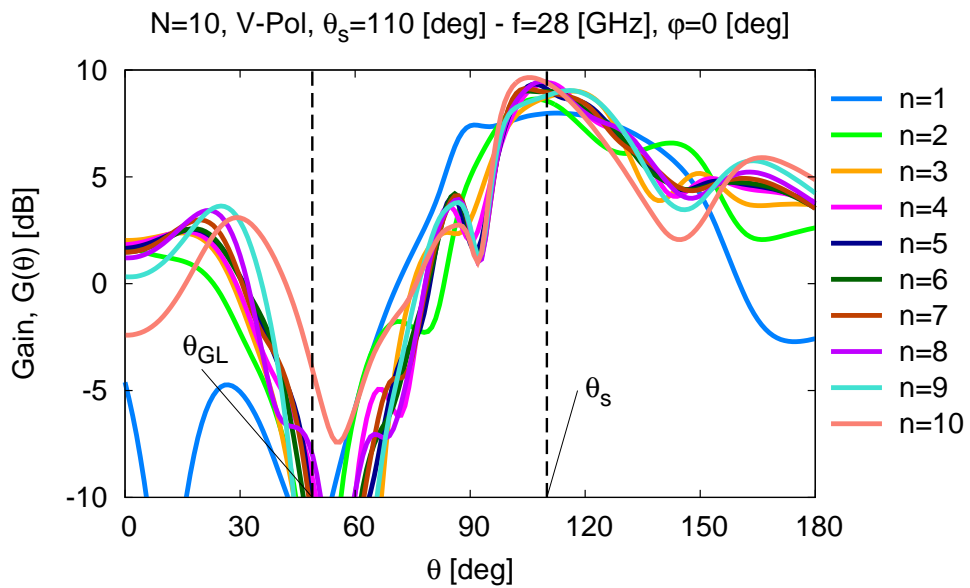


Fig. 16 - A. Benoni et al., "Co-Design of Low-Profile Linear Microstrip Arrays ..."



(a)



(b)

Fig. 17 - A. Benoni et al., "Co-Design of Low-Profile Linear Microstrip Arrays ..."

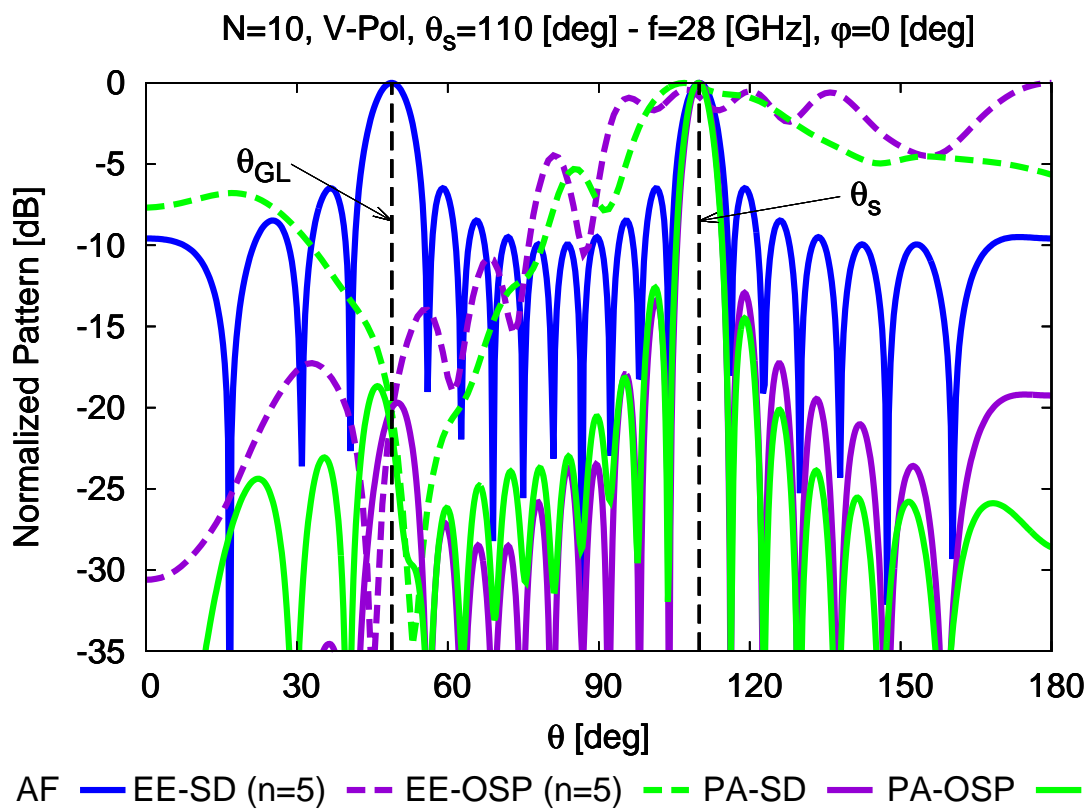


Fig. 18 - A. Benoni et al., “Co-Design of Low-Profile Linear Microstrip Arrays ...”

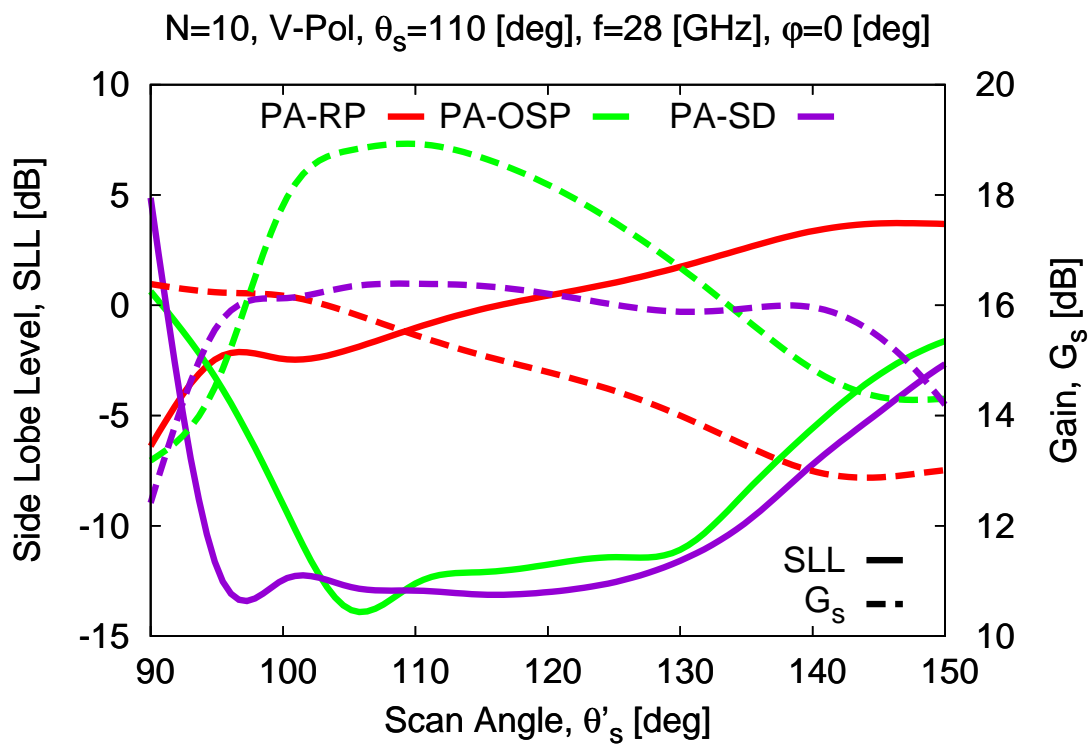
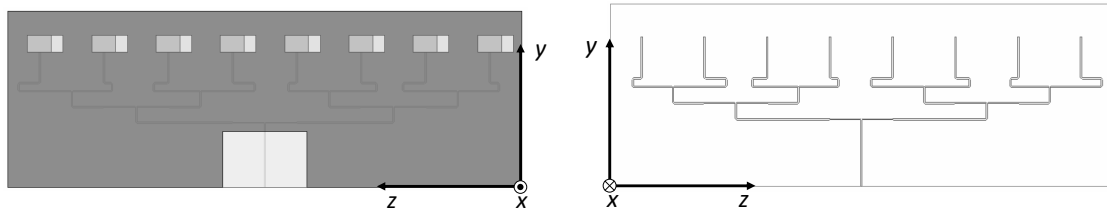
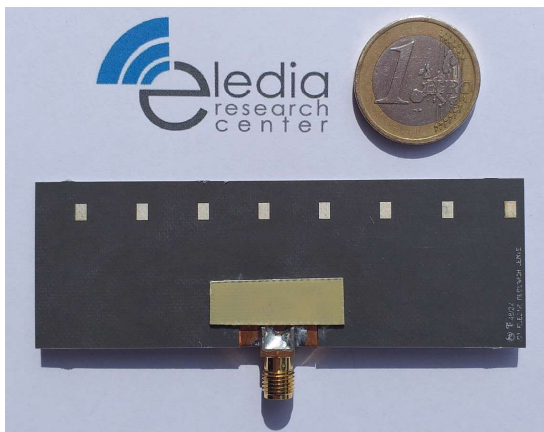


Fig. 19 - A. Benoni et al., "Co-Design of Low-Profile Linear Microstrip Arrays ..."

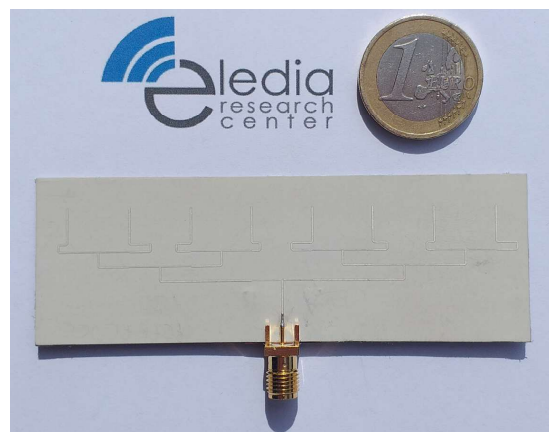


(a)

(b)

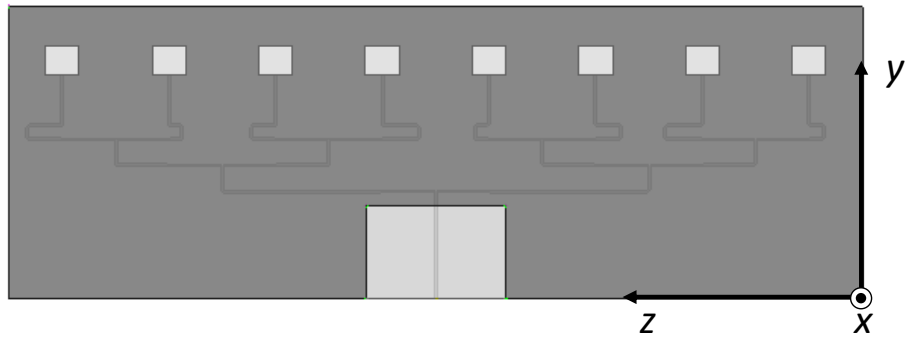


(c)

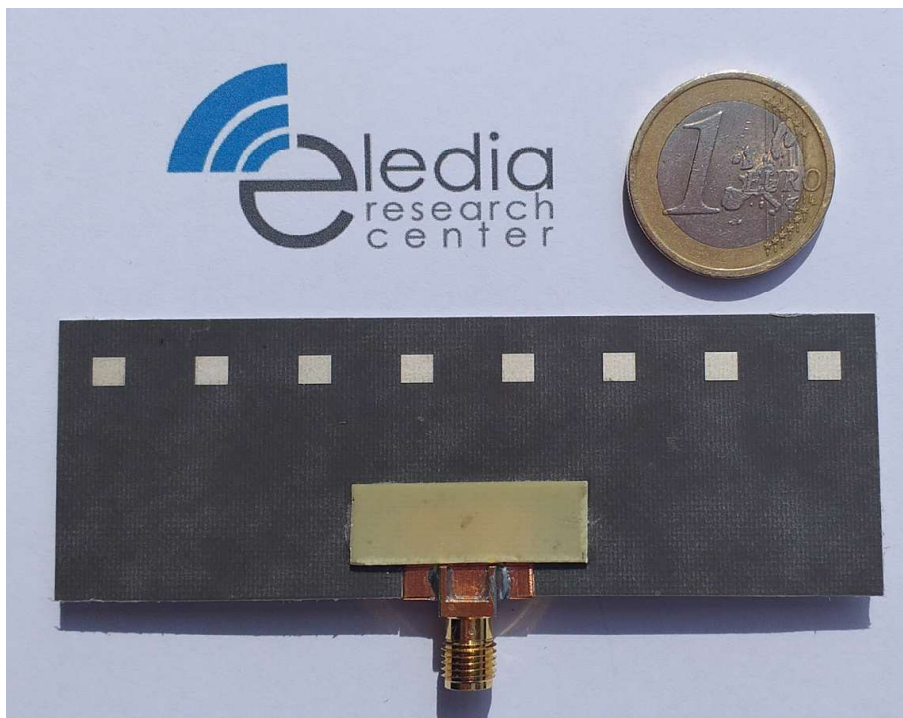


(d)

Fig. 20 - A. Benoni et al., “Co-Design of Low-Profile Linear Microstrip Arrays ...”



(a)



(b)

Fig. 21 - A. Benoni et al., "Co-Design of Low-Profile Linear Microstrip Arrays ..."

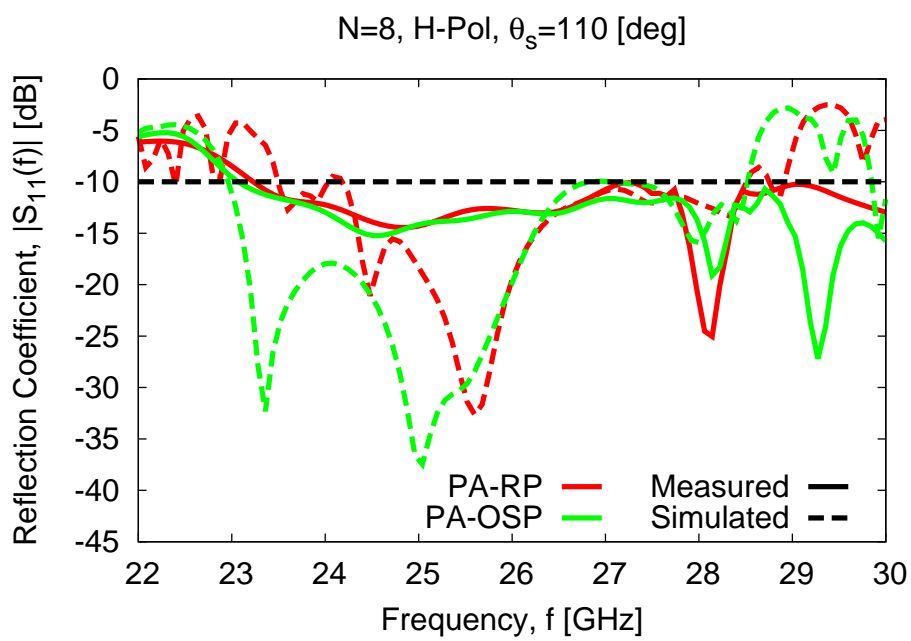
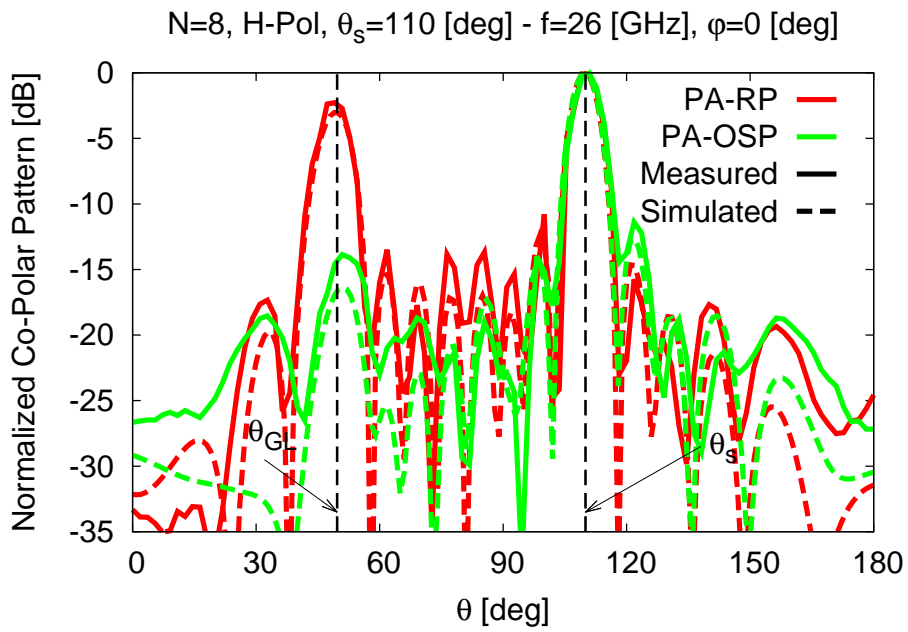
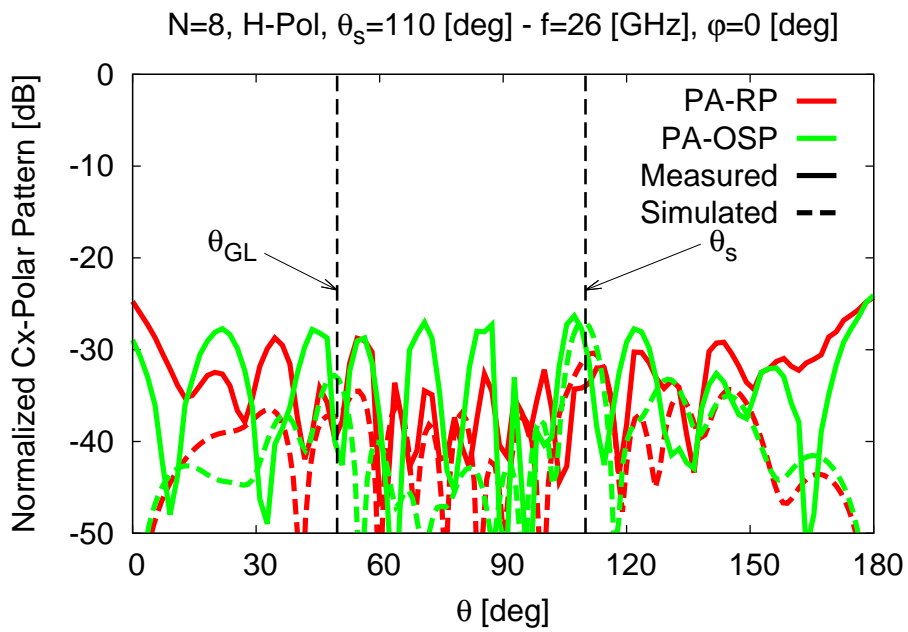


Fig. 22 - A. Benoni et al., “Co-Design of Low-Profile Linear Microstrip Arrays ...”



(a)



(b)

Fig. 23 - A. Benoni et al., "Co-Design of Low-Profile Linear Microstrip Arrays ..."

k	DoF	$H\text{-Pol}$ [m] (Fig. 5)	$V\text{-Pol}$ [m] (Fig. 16)
1	L_f	4.63×10^{-3}	4.63×10^{-3}
2	W_f	3.14×10^{-4}	3.56×10^{-4}
3	L_s	2.42×10^{-3}	2.43×10^{-3}
4	W_s	4.80×10^{-4}	4.79×10^{-4}
5	O_s	7.27×10^{-4}	7.26×10^{-4}
6	L_p	2.54×10^{-3}	2.64×10^{-3}
7	W_p	4.83×10^{-3}	4.86×10^{-3}
8	L_d	2.63×10^{-3}	2.70×10^{-3}
9	W_d	4.05×10^{-3}	4.46×10^{-3}
10	Δ_z	2.83×10^{-3}	3.35×10^{-3}

Tab. I - A. Benoni et al., “Co-Design of Low-Profile Microstrip Arrays ...”

<i>Test Case</i>	<i>Polarization</i>	<i>N</i>	<i>Antenna</i>	<i>SLL</i> [dB]	<i>G_s</i> [dB]
Fig. 6(a)	<i>H</i> -Pol	3	<i>PA-RP</i>	-2.96	12.44
Fig. 6(a)	<i>H</i> -Pol	3	<i>PA-OSP</i>	-12.45	13.41
Fig. 12(a)	<i>H</i> -Pol	5	<i>PA-RP</i>	-3.23	14.60
Fig. 12(a)	<i>H</i> -Pol	5	<i>PA-OSP</i>	-13.00	15.60
Fig. 12(b)	<i>H</i> -Pol	10	<i>PA-RP</i>	-3.60	17.65
Fig. 12(b)	<i>H</i> -Pol	10	<i>PA-OSP</i>	-14.57	18.72
Fig. 17(a)	<i>V</i> -Pol	10	<i>PA-RP</i>	-1.02	15.43
Fig. 17(a)	<i>V</i> -Pol	10	<i>PA-OSP</i>	-12.85	18.92
Fig. 18	<i>V</i> -Pol	10	<i>PA-SD</i> [1]	-12.93	16.39

Tab. II - A. Benoni et al., “Co-Design of Low-Profile Microstrip Arrays ...”